Controlled Properties of Gold Nanoparticles by CTAB Reverse Micelles and their Photothermal Effect in Human Cervical Cancer (HeLa) Cells

Valentina Guerrero Florez

Trabajo de Grado para Optar el título de Químico

Director
Fernando Martínez Ortega
Ph.D. en Química

Codirector
Stelia Carolina Méndez Sánchez
Ph.D. en Ciencias Bioquímicas

Universidad Industrial de Santander
Facultad de Ciencias
Escuela de Química
Bucaramanga
2019

Acknowledgements

This work would not have been possible without the financial support of Universidad Industrial de Santander-UIS (project 2303) and of the Administrative Department of Science, Technology and Innovation (Colciencias) for the postdoctoral research fellowship (“*Es tiempo de volver”*) cooperation agreement No. FP44842-507-2014.

I wish to present my special thanks to my advisors, Prof. Dr. Fernando Martínez Ortega, Prof. Dr. Stelia Carolina Méndez S. and Dr. Diana Blach for gave me noteworthy advises.

I would like to show my gratitude to Dr. Vicente Rodríguez González and Dr. Araceli Patron Soberano from the Instituto Potosino de Investigación Científica y Tecnológica (IPICYT), San Luis Potosí, S. L. P., México, for his generosity by allowing the microcopy experimentation of this work in the Division de Biología Molecular and Division de Materiales Avanzasdos at the IPICYT.

I do wish to express my thankfulness to my parents, Guillermo and Olga María, my sister, Linna Stefania and my partner, Dr. Jorge Mario. They have supported me in my academic and professional growth and have motivated me to perform all my activities with love, devotion and effort.

Table of Contents

Pag.

List of Figures

List of Appendices

Resumen

Título: Síntesis Controlado de Nanopartículas de Oro por Micelas Inversas de CTAB y su Efecto Fototérmico Sobre la Línea Celular de Cáncer Cervical Humano (HeLa)*

Autor: Valentina Guerrero Florez**

Palabras Claves: Nanopartículas de oro, micelas inversas de CTAB, irradiación láser, efecto fototérmico, especies reactivas de oxígeno, ácido fólico.

Descripción: La terapia fototérmica mediada por nanopartículas de oro (AuNPs) ha mostrado un creciente interés debido a que es una alternativa para la ablación efectiva de las células cancerosas. Sin embargo, la respuesta fototérmica de AuNPs debe adaptarse para mejorar la eficacia terapéutica y mitigar los efectos secundarios. En este estudio, evaluamos el efecto fototérmico de AuNPs esféricos y anisotrópicos con diferentes tamaños sintetizadas a través de micelas inversas de CTAB y AuNPs conjugadas con ácidos fólico (FA-AuNPs) en la línea celular de Cáncer de Cuello Uterino Humano (HeLa). Mostramos que los AuNPs con tamaños más grandes producen un calentamiento fototérmico mayor que aquellos que tienen tamaños más pequeños. Particularmente, los AuNPs anisotrópicos de 20 nm exhiben un potencial de uso como agentes fototérmicos debido a que mostraron una reducción de la viabilidad celular hasta el 60% a una concentración de 100 µM. Adicionalmente, revelamos que además del daño celular fototérmico, se forman altas concentraciones de especies reactivas de oxígeno (ROS) dentro de las células irradiadas. Inesperadamente, también mostramos que los FA-AuNPs inducen la muerte celular mientras disminuyen las ROS formadas durante el tratamiento de irradiación, protegiendo así las células no tratadas y disminuyen los efectos desfavorables de la formación de ROS. El efecto sinérgico de AuNPs y FA-AuNPs en el daño celular fototérmico con el daño producido por ROS concomitante inducido por el estrés térmico se corroboró usando ensayos de viabilidad celular, TEM y ensayos de fluorescencia. Los resultados sugieren la capacidad de las AuNPs generadoras de ROS para sensibilizar las células cancerosas y hacerlas vulnerables al daño fototérmico, así como el papel protector de las FA-AuNPs frente a la formación excesiva de ROS, proporciona un enfoque para optimizar la terapia fototérmica basada en AuNPs, permitiendo una mejora en la eficacia de los agentes fototérmicos.

---

* Trabajo de grado

** Facultad de ciencias. Escuela de Química. Director: Fernando Martínez Ortega, Ph.D. Codirector: Stelia Carolina Méndez Sánchez, Ph.D.

Abstract

Title: Controlled Properties of Gold Nanoparticles by CTAB Reverse Micelles and their Photothermal Effect in Human Cervical Cancer (HeLa) Cells*

Author: Valentina Guerrero Florez**

Keywords: Gold nanoparticles, CTAB reverse micelles, laser irradiation, photothermal effect, reactive oxygen species, folic acid.

Description: Gold nanoparticle (AuNPs)-mediated photothermal therapy has shown a growing interest due to promise alternative for the effectively ablation of cancer cells. However, the photothermal response of AuNPs must be tailored to improve the therapeutic efficacy of plasmonic photothermal therapy (PPT) and mitigated concerns regarding side effects. In this study, we utilized laser-treated spherical and anisotropic AuNPs with different size synthetized via CTAB reverse micelles and biocompatible folic acid (FA)-conjugated AuNPs (FA-AuNPs) in well-known human epithelial cervical cancer cell line (HeLa) as an alternative to facile tunability photothermal efficacy and target selectivity. We show that AuNPs with larger sizes produced more photothermal heating effect than those having smaller sizes. Particularly, 20 nm anisotropic AuNPs successfully demonstrate potential for use as photothermal agent, showed a reduced viability down to 60% at a concentration of 100 μM. Furthermore, we disclosed that in addition to the photothermal cell damage, high concentrations of reactive oxygen species (ROS) are formed within the irradiated cells. Unexpectedly, we also show that the FA-AuNPs inducing cell death while diminished the ROS formed during PPT treatment, thereby protecting untreated cell and diminish unfavorable sequelae effects from ROS formation. The synergistic effect of AuNPs and FA-AuNPs in effectively photothermal cell damage with the concomitant heat stress induced ROS during irradiated-treatment was corroborated using cell viability, TEM, and fluorescence assays. Our results suggest that the ability of ROS-generating AuNPs to sensitize cancer cell and make them vulnerable to photothermal damage as well as the protective role of FA-AuNPs from excessive ROS formation provides an approach to optimize AuNPs-based photothermal therapy, allowing an improvement in the efficacy of PPT agents while reducing repeated exposures to high temperatures required to induce thermal stress.

---

* Bachelor Thesis

** Facultad de ciencias. Escuela de Química. Advisor: Fernando Martínez Ortega, Ph.D. Co-Advisor: Stelia Carolina Méndez Sánchez, Ph.D.

Introduction

The well-known intrinsic limitations of conventional cancer therapies have rocketed the advances in the field of nanoscience, providing a unique approach and a comprehensive technology against cancer. Thus, the development of noble metal nanostructures with unique features (such as optical, magnetic, electric and structural properties) is the main goal in the manufacture of therapeutic agents. The growing interest in applying nanotechnology to cancer is large because of its unique features that have been studied in, e.g., diagnosis (Mieszawska, Mulder, Fayad, & Cormode, 2013), targeted drug delivery (Gu et al., 2007), image contrast agent (Loo et al., 2005), and therapeutic nature of some nanomaterials themselves (Misra, Acharya, & Sahoo, 2010). In this regard, the gold nanoparticles (AuNPs) are outstanding photothermal agents for cancer therapy applications because they exhibit efficient local heating after direct excitation of surface plasmon oscillations (SPR); because the light is strongly absorbed and then quickly converted to heat by a series of non-radiative processes. Furthermore, the strong absorption, the efficient heat conversion via non-radiative processes, the high photostability and the inherent low toxicity contribute to the increasing interest in killing cancer cells via hyperthermia using AuNPs, namely plasmonic photothermal therapy (PPT) (J. Song et al., 2014).

Beyond using gold nanomaterials as a PPT agent, some studies have observed that reactive oxygen species (ROS) come when noble metal nanostructures are irradiated by employing either continuous-wave (CW) or pulsed laser. (Pasparakis, 2013; Yoo et al., 2012). In particular, it was reported that spherical metal NPs including Au, Ag, and PtNPs, are able to sensitize the formation of ROS upon visible light excitation (Vankayala, Sagadevan, Vijayaraghavan, Kuo, & Hwang, 2011). The exact mechanism leading to ROS production is poorly understood. However, it has been established that ROS can be produced in response to heat stress during PPT treatment (Aioub, Panikkanvalappil, & El-Sayed, 2017). ROS is known to play an essential role in the photodynamic therapy (PDT), where the activation of an organic photosensitizer by the light of an appropriate wavelength the light energy to oxygen in tissue, generates ROS in the form of free radicals or singlet oxygen (Celli et al., 2010). This organic or organometallic dyes are prone to photoinduced degradation and enzymatic degradation, which becomes in drawback to PDT treatments and limit their biomedical applications (Batchelor, 2008). To overcome these limitations many researchers have developed a strategies to combine simultaneously several to produce multifunctional nanostructures such as gold nanorod-photosensitizer complexes (Jang, Park, Tung, Kim, & Choi, 2011; Kuo, Chang, Cho, Chiu, Lien, Yeh, & Chen, 2012) to achieve both PDT and PPT. Therefore, AuNPs are expected to be better ROS photosensitizers than conventional organic dyes due to its superior photostability and resistance to enzymatic degradation (Vankayala et al., 2013).

The effectiveness of AuNPs as therapeutic agents strongly depends on their optical and photothermal properties, thereby controlling the synthesis plays a key role in achieving a localized heating and therefore, a successful PPT. In this sense, our effort focused on synthesizing AuNPs controlling the geometry, the optical and surface chemical properties to improve their features as *nanoheaters*. To achieve this goal, reliable wet synthetic method known as a Reverse Micelle (RMs) were studied. RMs can be described as “nanoreactors” because they bridge the non-polar and polar phases and provided a suitable and unique environment for controlling many proprieties of the synthesis. A control over the nucleation and growth process has been observed varying the composition of microemulsion (Cason, Miller, Thompson, & Roberts, 2001; Chiang, Hsu, & Lai, 2004; Kitchens, McLeod, & Roberts, 2003; M. S. Lee, Park, Lee, Ju, & Hong, 2005).Therefore, in this work, we assess the effect of the different molecular structure of organic solvents in the RMs used as AuNPs reactors in two CTAB-stabilized reversed micellar systems, i.e, toluene/1-butanol/CTAB/water and *n*-hexane/1-butanol/CTAB/water. Handling these attributes, we can modulate the proportion of light scattering relative to light absorption for the intended application by varying size and/or shape. In order to localize heating mediated by AuNPs using laser light, we are planning to modify the surface of the nanoparticles with folic acid (FA) to ease their cellular uptake. Finally, those are going to be evaluated on human cervical cancer HeLa cells as potential PPT agents.

This document is organized as follows: First section exposes the foundations and the most outstanding studies in the literature related to this work. Second section shows the synthetic procedure of AuNPs, the studies carried out in CTAB RMs and the *in vitro* implementation of AuNPs as a PPT agent in HeLa cells. Finally, the document concludes detailing the most relevant inferences of the entire document.

1 Objectives

1.1 General objectives

Evaluate the photothermal effect of two types of AuNPs (i.e., spherical and anisotropic) obtained via CTAB reverse micelles as a mediator of cell death in human cervical cancer HeLa cells.

1.2 Specific objectives

i) To study the effect of the CTAB reverse micelles composition in the micellar exchange dynamics on the size and shape properties of the synthesized AuNPs.

ii) To evaluate the *in vitro* biocompatibility of AuNPs in human cervical cancer HeLa cells by means of cell viability assays.

iii) To characterize the photothermal effect over human cervical cancer HeLa cells treated with biofunctionalized and non-biofunctionalized AuNPs.

2 Literature review

2.1 Nanotechnology and medicine

Nanotechnology has emerged as a multidisciplinary science involved in the design, synthesis, characterization and application of materials and devices whose dimensions are in the domain of atoms and molecules sizes, ranging from a few to several hundred nanometers. Its efforts have focused to obtain a fundamental understanding of optical, electrical, magnetic and mechanical properties of nanostructures, with respect to their size, shape, and surface chemical (Albanese, Tang, & Chan, 2012). Over the past three decades, there are several areas of science and technology where nanomaterials are under active development or already in use, e.g., microelectromechanical, electronic and biomedical devices (SCENIHR, 2006). The field of nanotechnology continues to grow remarkably: the ability to modify properties of matter by changing the interphase features has given rise to investigate the interactions of nanomaterials with biological systems, because it offers approaches to test and control several biological processes that occur at nanometer scales. Among the nanomaterials currently used, nanoparticles of noble metals are the most extensively studied due to their unique properties, whose have led to new interesting developments with a profound impact on disease prevention, diagnosis and treatment (Sau, Rogach, Jäckel, Klar, & Feldmann, 2010). It is important to highlight that nanoparticles provide substantive advantages for designing and tuning properties, which is impossible to obtain with other types of therapeutic drugs, showing a bright future as a new generation of cancer therapeutics (Misra et al., 2010). Thereby, a question arises: What physicochemical properties make the noble metal nanoparticles such appropriate structures?

2.2 Metal nanoparticles: physical and chemical properties

Nanoscale materials often demonstrate an intermediate behavior between a macroscopic solid and an atomic (or molecular) system. When a small spherical metallic nanoparticle is irradiated by light, the oscillating electric field causes the conduction electrons to oscillate coherently, known as localized surface plasmon resonances (LSPR). These optical and electronic properties of metal nanoparticles have been of interest for a long time. Scientific researches date, at least, to the synthesis of colloidal gold performed by Michael Faraday in the mid-1850s, who for the very first time announced that the interaction of light with particles of different morphologies gave rise to the color (Faraday, 1857). In 1908, Gustav Mie solved Maxwell's equations to describe the light interaction with spheres of arbitrary radii and compositions, from the red color observation of the gold nanoparticles in a solution, assuming sphere sizes comparable to the wavelength (Bancroft & Gurchot, 2005; Mie, 1908). Subsequently, based on the results of Rayleigh, who found a solution to the problem for a sphere smaller than the light wavelength and those sizes obtained by Mie, Gans finally demonstrated that the optical response of metal nanoparticles with elliptical geometries depends largely on their shape (Gans, 1912). He also explained the origin of the color differences from a colloidal nanoparticle's solution with different aspect ratios.

Doubtlessly, the noble metal nanoparticles have been widely studied, especially gold nanoparticles (AuNPs), which have recently attracted considerable attention because of their multiple interesting optical properties which render them as ideal candidates for a wide range of applications, for example, in catalysis (Thompson, 2007), surface enhanced spectroscopies (Langer, Novikov, & Liz-Marzán, 2015), energy (de Aberasturi, Serrano-Montes, & Liz-Marzán, 2015) and health (X. Wang, Yang, Chen, & Shin, 2008). Furthermore, their increasing attention is also attributed to their tunable optical (plasmonic) properties.

2.3 Gold plasmonic properties

The physical origin of the light absorption by metal nanoparticles is the coherent oscillation of the conduction band electrons induced by the interacting electromagnetic field, as stated above. When the conductor dimensions are reduced, regarding that most of the atoms are located on the surface, the optical properties of small metal nanoparticles are dominated by the collective oscillation of conduction electrons (Metiu, 1984). The excitation of LSPR occurs in the visible and near-infrared regime of the spectrum for gold nanoparticles, which are mainly governed by their shape and size (Kelly, Coronado, Zhao, & Schatz, 2003).

The strong absorption and scattering of AuNPs, coupled with advances in nanoparticles synthesis, conjugation and assembly, have been employed in diverse biomedical applications, as Figure 1 shows. For instance, the dependence of the plasmon band position on the aggregation degree of the nanoparticles produced by molecules adsorbed to the surface, forms the basis for chemical sensing with gold nanoparticles (C. Lin, Lee, Hsieh, & Wang, 2009). It can lead to a single molecule detection and identification to being used as a surface-enhanced Raman spectroscopy (SERS) substrate for targeted detection (ANKER et al., 2009). Under direct excitation (or LSPR), AuNPs transfer efficiently the energy (heat) to the surrounding media throughout a cascade of events (P. K. Jain, Huang, El-sayed, & El-sayed, 2008). The resulting light absorption creates intense localized heating, which is the basis of the plasmonic photothermal therapy.

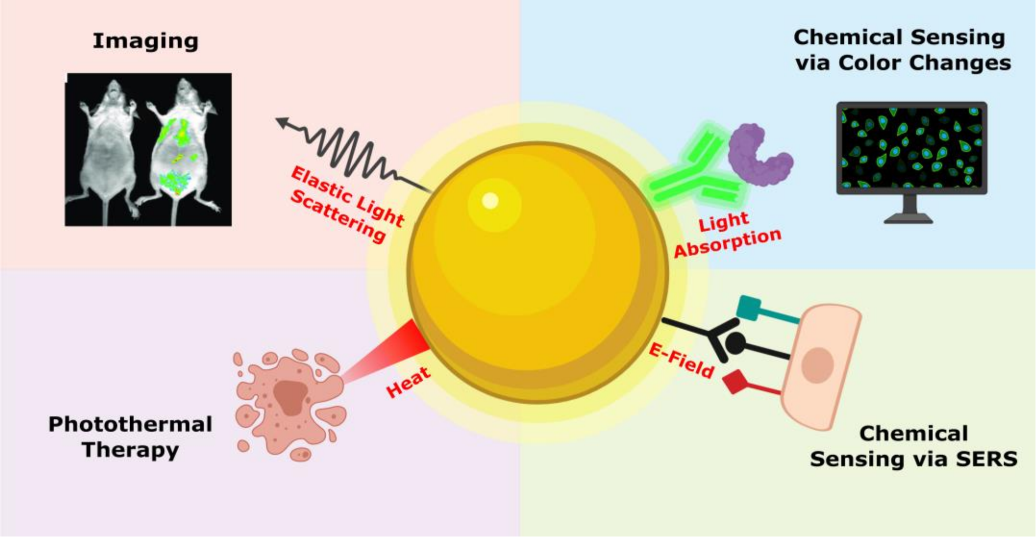

Figure 1. Schematic representation of the physical event that occurs when a light interacts with a nanoparticle. The presence of scattering, luminescence and heat generation are included, with the corresponding application.

Nowadays, nanoparticles can be synthesized reproducibly, modified with chemical functional groups, and characterized by several analytical techniques, which have allowed to know up to an atomic level precision the conformation of these materials. Nevertheless, the major contribution to the development of this field was made on the design, control and functionalization of nanostructures. The microemulsion method has been one of the most noteworthy and novel routes to tailor nanoparticles. In this sense, in the following section, we give a brief introduction to the basic concepts of microemulsions, their applications into nanomaterial synthesis and some of the most important contributions in the literature. Additionally, we also review one of the most extensively studied molecules targeting, the folic acid (FA), used in the nanoparticle functionalization procedure.

2.4 Synthesis of nanoparticles in microemulsions

Several methods for the synthesis of gold nanoparticles have been developed in the recent years in the search for modulating the final properties of nanoparticles, among them it is the one based on microemulsions (J. Lin, Zhou, letters, & 2001, n.d.; V. R.-R. C. Reviews & 2000, n.d.; Schmitt, Mächtle, Eck, Möhwald, & Helm, 1999; Wilcoxon, Williamson, & Baughman, 1993). Microemulsions are used as chemical reactors due to their hydrophilic and hydrophobic features, specially their interfacial properties. A microemulsion is a thermodynamically stable dispersion of two immiscible fluids containing an appropriate amount of surfactant. Different types of microemulsion have been used as chemical reactors at the nanoscale level, e.g., the "water-in-oil" (w/o) microemulsions formed when water is dispersed in a hydrocarbon-based continuous phase surrounded by a monolayer surfactant that stabilizes the dispersion and, in presence of a cosurfactant, as a surfactant assembly. This thermodynamically driven assembly generates aggregates known as reverse or inverted micelles (RMs), which are widely used today in the synthesis of many types of nanoparticles (M. López-Quintela, Rivas, Blanco, materials, & 2004, n.d.; Myakonkaya et al., 2009).

2.5 Formation mechanism and growth control

RMs can be described as "nanoreactors" providing a suitable environment for controlled nucleation and growth. In addition, it has been observed that many properties of the synthesized can be controlled varying the microemulsion composition, because lately it has been considered as the most important factor that influences the final product morphologies and properties

(USKOKOVIĆ & DROFENIK, 2005). Therefore, the dynamic feature of these nanoreactors must be taken into account for an understanding of the chemical reactions carried out in these media.

The interaction of the surfactant polar headgroups with the polar solvent and cosurfactant can result in the formation of a defined solvent pool, where reactants are solubilized in separate micellar solutions to react upon mixing. The micelle core size is described by the molar ratio of water to surfactant molecules in the solution, W_0 = [water]/[surtactant], and defined as the molar ratio of water-to-surfactant. Thence, the material exchange takes place by following the mechanism shown in Figure 2. The RMs droplets collide among themselves forming a water channel that results in a transient dimer formation followed by a droplet fusion, to exchange the reactants and break them apart again (A. Reviews & Langevin, 1992). Once such a dimer is formed, the intermicellar exchange of the reactants takes place and then, the nucleation starts at the micellar edges with the well-known growth process (Ganguli, Ganguly, & Vaidya, 2010). Naturally, it is possible to anticipate that the interfacial properties as well as the RMs composition play an important role in the nucleation and growth processes. For instance, it has been demonstrated that by changing the RMs composition also modifies the droplet size and the interdroplet interaction (Hou, Kim, & Shah, 1988), and in turn, the attraction between droplets also depends on the interfacial fluidity (Cazabat & Langevin, 1981). The interfacial fluidity denotes the bending modulus (elasticity/rigidity) of the surfactant film and depends on the surfactant type, cosurfactant and oil used as well as on the droplet size (Eastoe, Hollamby, & Hudson, 2006a). Some properties that have been reported to influence the size and polydispersity of nanoparticles synthesized inside RMS are the type of solvent employed, the surfactant or co-surfactants used, and the impurities added (D Blach, Correa, Silber, science, & 2011, n.d., pp. 4–10; De, science, & 1995, n.d., p. 5).

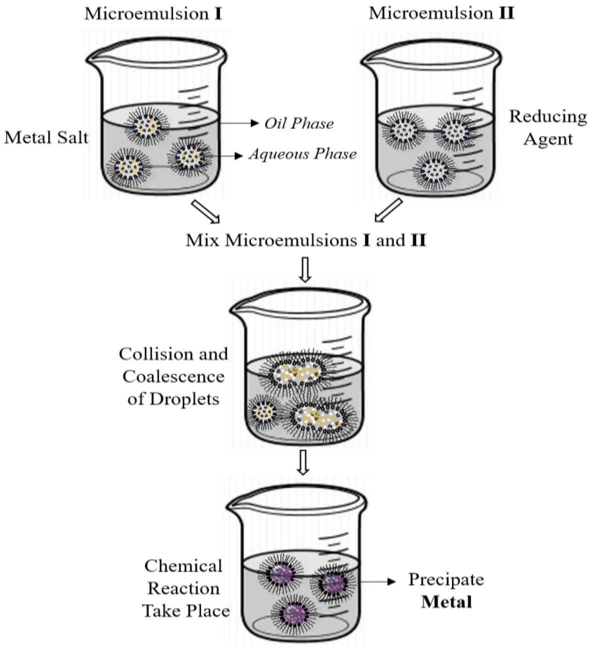

Figure 2. Illustration of the intermicellar exchange process. Based on (Eastoe, Hollamby, & Hudson, 2006b).

Nevertheless, the interdroplet interaction plays a predominant role in the final properties of nanoparticles, then it is also crucial to understand the nature of the RMs interface because mass transfers are not possible unless the interface is disrupted (García-Río, Godoy, & Rodríguez-Dafonte, 2006). On the one hand, interesting RM interfacial properties have been investigated in anionic sodium 1,4-bis (2-ethylhexyl) sulfosuccinate (AOT) reverse micelles (RMs) by Gutierrez et al. (2014) in the synthesis of AuNPs. The Authors found that the change of the nonpolar organic composition in a *n*-heptane:benzene/AOT/water RMs media, modulates the interdroplet interaction and, as a result, several AuNPs with different size and shape can be found. Particularly, AOTs have been intensively developed due to these systems are well characterized (García-Río et al., 2006). Similarly, the influence of organic media composition has been investigated for the cationic RMs formed with the benzyl-*n*-hexadecyltrimethylammonium chloride (BHDC) surfactant (Federico M. Agazzi, R. Dario Falcone, Juana J. Silber, 2011). On the other hand, few studies have been performed to explore the role of cationic CTAB RMs in the AuNPs synthesis (F. Chen, Xu, & Hor, 2003).

2.6 CTAB microemulsions

The cationic surfactant cetyltrimethylammonium bromide (CTAB) has been used in the RMs formulation because it shows remarkably more solubilization capacity of high aqueous salt solution concentration than AOT systems. Such a fact provides a very flexible film, which gives a high exchange dynamic of the micelles, elliptical and spherical CTAB micelles, known to be able to coexist (Fang & Yang, 1999). In general, these sorts of linear surfactants tend to form ellipsoidal micelles when the surfactant has tails of moderate length between C_{10}-C_{16}. Note that, as Figure 3 shows, CTAB is a C_{16} surfactant thought to be spherical (or nearly spherical) close to critical micellar concentration (CMC). The formation of these micelles is an entropy driven process, thereby CMC is the concentration of surfactant molecules organized spontaneously to form aggregates such as micelles, vesicles (Ganguli et al., 2010), CTAB as $CMC_1 \approx 0.92$ mM and $CMC_2 \approx 270$ mM in water (Lutz-Bueno, Pasquino, Liebi, Kohlbrecher, & Fischer, 2016). It is important to highlight that for CTAB reverse micelles a co-surfactant is certainly required for the formation of a stable microemulsion (Gómez-Graña et al., 2012).

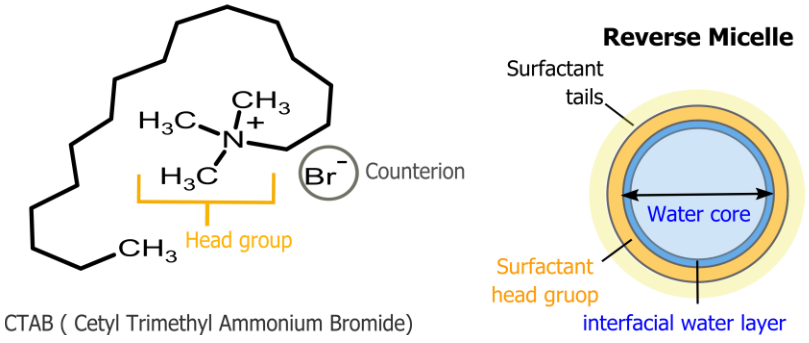

Figure 3. Feature of CTAB molecule and a schematically representation of CTAB reverse micelle.

Porta et al. (2002) obtained AuNPs as small as the reactant concentration increases by using CTAB/n-octane/1-butano. They discussed the possibility that alcohol behaves as a capping agent at high concentrations. Chen et al. (2000) studied the influence of both reactants, metal salt and reducing agent, on final Ni nanoparticle size and number in a water/CTAB/n-hexanol microemulsion. In the CTAB/n butanol/isooctane/water microemulsion system, the effect of microemulsion compositions revealed that the key factor affecting the size of palladium nanoparticles was the interfacial property, determined by the ratio of CTAB to n-butanol (C. C. Wang, Chen, & Huang, 2001). This kind of microemulsions have also been used to produce other materials, such as spinel, perovskites and coated materials like SiO_2 coated Pt, Pd and Pt/Ag (M. A. López-Quintela, Tojo, Blanco, García Rio, & Leis, 2004). These findings certainly confirm that the properties and composition of the RMs can be varied to modulate the final properties of synthesized materials in these systems.

2.7 Gold nanoparticles as a therapeutic agent

2.7.1 Cytotoxicity. Regarding the cytotoxic effects, they must be distinguished between the effects related to the nature of the material and the common ones to nanoparticles of even inert materials. Although, gold nanoparticles are composed of an inert material, then biocompatibility issues must be considered. In in vitro assays, AuNPs are considered as biocompatible and acute cytotoxicity has not been observed yet (Yang, Sun, Chiu, Sun, & He, 2005). Chithrani et al. (2006) found that the cells exposed to gold nanoparticles were incorporated and located inside the cells in vesicular structures close to the cell nucleus. In general, there are few examples of toxic effects related to the nature of gold, which depend on the chemical functionality and charge, and the size of the nanoparticles. However, gold nanoconjugates functionalized with CTAB were initially thought to be toxic, but it was subsequently determined that the particles do not cause cytotoxicity if they are washed to remove the ligand excesses (Connor, Mwamuka, Gole, Murphy, & Wyatt, 2005). Likewise, DNA-AuNPs (or amine-functionalize) have been shown to possess cytotoxicity lower than the polymer systems (Rosi et al., 2006). Notwithstanding, Au55 clusters have been demonstrated to fit into the DNA molecule grooves and thus cause cytotoxic effects (Tsoli, Kuhn, Brandau, Esche, & Schmid, 2005). In most of the studies about nanoparticle toxicity, the surface functionalization has repeatedly been proved to be the key parameter that influences toxicity.

3.7.2 Surface modification of gold nanoparticles using folic acid. Interaction of nanoparticles with human cells is an interesting topic for understanding toxicity and develop potential therapies, with the goal of improving the therapeutic efficacy. The surface on nanoparticles can be conjugated with biomolecules and other chemical compounds. One of the most promising agent targetings is folic acid (FA), it has been studied extensively as an optimal targeting ligand for imaging and cancer therapy over the last two decades (Turk, Reddy, Chmielewski, & Low, 2002). Furthermore, its attractive properties including stability, small size, low cost, poor immunogenicity, and specificity for pathologic cells (G. Li, Li, Zhang, Zhai, & Wang, 2009).

FA is one member of the vitamin B complex and is required in several metabolic pathways because it is assisting in the biosynthesis of nucleic acids and amino acids, whereby plays a vital role in tissue growth, the vitamin is consumed in elevated quantities by proliferating cells (Antony, 1992). Folate receptors (FRs) are frequently overexpressed in many of the human cancerous cells, perhaps enabling the malignant cell to compete successfully for the vitamin when supplies are limited, they are only minimally distributed in normal tissues (Lu & Low, 2012). Folate specifically binds to FRs with a high affinity (KD = ~ 10^{-9} M), enabling many works that discussed medicated nanomaterials with FA for specific targeting and the improvement uptake by cancer cells through FR mediated endocytosis (Gu et al., 2007; Lu & Low, 2012; Sun, Sze, & Zhang, 2006). Despite the works on FR-target nanoparticles system it needs to be studied thoroughly to increase tumor selectivity. Despite the many works on utilizing FA on nanoparticles for the active targeting of cancer cells overexpressing folate receptors (Taira et al., 2007; Teow & Valiyaveettil, 2010), it should be thoroughly studied to increase tumor selectivity and to know the action pathways have not yet been reported.

2.7.3 Hyperthermia treatments. Hyperthermia is a medical treatment in which cancer cells (or tissues) are heated to with a temperature slightly higher than normal conditions, above 41-48 ºC, for a period of a few minutes, in order to annihilate them (Svaasand, Gomer, & Morinelli, 1990). Cancer cells can be selectively destroyed due to tumor tissues have abnormal vascular structures, which causes a difficult heat dissipation and, so hyperthermia sensitivity greater than that of healthy tissue (C. W. Song, 1984). Biological processes underlying the hyperthermia treatments have been attributed to drastic activation of cell death as a consequence of coagulative necrosis processes. In the 41–48 ºC temperature range, several processes of relevance at the cellular level are simultaneously activated. It is well known that when the cellular temperature exceeds 39 ºC, the protein denaturation starts. As a result of denaturation, proteins are prone to aggregation and the subsequent aggregates can have destructive consequences in the cell dynamics and survival rates. These biological pathways result in ablation of tumor tissues, since the effect of temperature is therefore considered as drastic and irreversible. Thence, this kind of treatment is considered highly efficient, but the cell death and the response of the cells exposed to high temperatures depend on both the exposure duration and the magnitude of the temperature (Jaque et al., 2014).

Furthermore, PTT is a slightly invasive hyperthermia treatment method in which the photon energy is converted into thermal energy to induce cancer hyperthermia. Recent developments of nanoparticles, which are capable of an efficient heat generation under illumination with laser radiation and can be used as photothermal agents, have attracted great attention for the last few years (Pissuwan, Valenzuela, & Cortie, 2006).

2.7.4 Plasmonic photothermal therapy (PPT) using gold nanoparticles. Nanotechnology has been explored news alternatives for localized heating based on the development of nanoparticles with outstanding thermal properties. Recent developments reported nanoparticles capable of efficient heat generation under illumination with laser radiation (Jaque et al., 2014). For instance, the AuNPs combined with photothermal therapy are efficient exogenous agents for cancer therapy (X. Huang, Jain, El-Sayed, & El-Sayed, 2008). When these agents absorb light, the SPL is excited causing a collective oscillation of electrons, then the excited electrons pass their energy to phonons by electron–phonon interactions of the order of 0.5 to 1 ps. Throughout interactions between the electrons and the crystal lattice of AuNPs, the electrons relax, and the thermal energy is transferred to the lattice. Straightforwardly, the heat from the gold nanoparticles is dissipated in the surrounding environment, with an increase in temperature of the order of a few tens of degrees. The electronic relaxation on a long-time scale has been studied by Hartland et al. and Vallee et al., who have attributed these oscillation behaviors to the breathing vibrational mode excitation of the nanoparticles because of the energy transfer from the “hot” electrons into the lattice via electron-phonon coupling (José H. Hodak, Martini, & Hartland, 2002; Jose H Hodak, Henglein, & Hartland, 2000).

Lastly, the controlled heating of gold nanoparticles can be used in several ways for manipulating the surrounding tissues (Parak, 2008). Hence, the photothermal response of gold nanoparticles, including nanorods, nanoshells, nanoclusters, and nanocages, has been exploited for the hyperthermia destruction of cancer cells (J. Song et al., 2014). Highlighting on nanoparticles able to mediate intermicellar hyperthermia in which plasmonic nanoparticles are internalized first by cells, followed by exposure to laser irradiation that induces an increase in temperature and, thus, leads to the cell death (H. C. Huang, Rege, & Heys, 2010).

3 Methodology

This research work aims at the synthesis and characterization of two types of gold nanoparticles (i.e., spherical and anisotropic) as possible hyperthermia agents in plasmonic photothermal therapy for the elimination of human cervical cancer HeLa cells.

3.1 Synthesis of AuNPs via CTAB reverse micelles

The stock solutions of CTAB in hexane and toluene (0.1 M) were prepared by mass and volumetric dilution, to obtain optically clear CTAB solution, 1-butanol as a cosurfactant was used. To determine the amount of alcohol required to form isotropic solution, CTAB was dispersed with an organic solvent to produce turbidity and then, 1-butanol 6.5 M and 3.3 M solution were added to the CTAB/hexane and CTAB/toluene solutions, respectively. The solution was shaken in a sonicating bath for approximately 10 min until getting a translucid solution. A calibrated microsyringe was used to introduce the aqueous solution into each micellar solution. The amount of water present in the system is expressed as the molar ratio between water and surfactant (i.e., W_0 = [water]/[CTAB]). The lowest value of W ($W_0 = 0$) corresponds to a system without the addition of water.

The methodology used to synthesize AuNPs in RMs is based on mixing two identical micellar solutions. A solution of hexane/1-butanol/CTAB/water ([CTAB] = 0.1 M) containing tetrachloroauric acid dissolved in water (0.05 M) at $W_0 = 6$ and another containing hydrazine (0.5 M) dissolved in water. The auric ions reduction process occurred when the two RM systems were mixed and, the nucleation and growth processes took place in a RMs polar core at room temperature.

The physical chemical properties of the RMs solutions were evaluated via FT-IR and ^{1}H NMR analyses, by using a Bruker FTIT and a Bruker ACP 300 MHz spectrometer. ^{1}H-NMR spectra were recorded in a digital resolution of 0.06 Hz per data point at 25 ± 0.5 °C. A capillary tube containing D_2O was introduced in the NMR tube and used as a “lock” frequency. Chemical shifts were measured to the D_2O signal and the obtained values were reproducible within 0.01 ppm. All NMR data were processed and plotted by using MestRe-Nova and Origin Pro 8, respectively, running on MS Windows 10.

The AuNPs growth was measured at 30 s of synthesis with different prepared samples, adding L-cysteine (0,03 M) as stabilized molecule. Particle growth was followed by UV-Visible spectroscopy, measured by a spectrophotometer Hewlett Packard-Agilent 8453 with a thermostatic sample holder. A path length of 1 cm was used in absorption experiments. Particle size measurements were carried out through transmission electron microscopy (TEM) at FEI TECNAI G2 STWIN at 20–200 kV with a camera Gatan ES100W and, a formvar-covered copper grid as a sample holder. The size distribution and average number of particle diameters were obtained using the Gatam Digital Micrograph

3.2 In vitro assays

3.2.1 AuNPs conjugation. Spherical AuNPs of 9-14 nm and anisotropic AuNPs of 15-20 nm stabilized with L-cysteines were synthesized via CTAB reverse micelles (RMs) well-known as a *nanoreactors*. All AuNPs solutions were purified by centrifugation for 20 min at 10000g and redispersed in deionized water twice to remove CTAB excesses. The AuNPs were then conjugated with FA to increase their stability and biocompatibility. A 1×10^{-3} M aqueous solution of FA at pH 11 (1 M NaOH) was added to the solid obtained in the precipitation and phase transfer process. Then, FA-AuNPs solutions were vigorously stirred for 30 min at room temperature and subsequently centrifuged (10000g, 20 min) to remove unbound FA molecules and dispersed in cells medium MEM. FA and FA-AuNPs solutions were analyzed by fluorescence spectroscopy with a Perkin Elmer's LS-55 spectrofluorometer by using an excitation wavelength of 364 nm. Measurements of Z-potential were carried out via a Zetasizer Nano's ZS90 equipment for each one of these solutions.

3.2.2 Photothermal heating of AuNPs solutions. Different AuNPs were diluted in cell culture media. An AuNPs solution of 1 mL was loaded into a standard quartz cuvette and then exposed using a ThorLabs' diode laser of 638 nm for increasing the irradiation times and the temperature measured by directly placing a thermocouple into solutions over 10 min of laser exposure. To ensure uniformity, the initial temperature of all solutions was 25 ± 1°C.

3.2.3 Cell culture and treatments with AuNP. HeLa cell line was obtained from American Type Culture Collection (ATCC, USA). Cells were maintained in Minimal Eagle Medium (MEM) supplemented with 7% v/v fetal bovine serum (FBS) and 1% v/v antibiotic under standard conditions at 37 °C and a humidified atmosphere containing 5% CO_2 and 95% air. From growth to confluency, cells were trypsinized, counted by utilizing a hemocytometer, and cultured into a fresh medium. For the experiments, cells were seeded at a density of $1x10^4$ cells/well on a 96-well plate in a volume of 200 µL containing EMEM supplemented medium at 37 °C, 5% of CO_2, and an atmosphere of 95% air for 24 h. Upon 70% of confluence, cells were exposed to various concentrations of AuNPs and FA-AuNPs (10, 50 and 100 µM) for 4 h. For PPT studies, cells were grown with the same conditions described above and after overnight incubation, the growth media was replaced by varying concentrations of AuNPs and FA-AuNPs (i.e., 10, 50 and 100 µM). After incubation for 4 h with AuNPs and FA-AuNPs and a subsequent replacement of the culture media (for removing free agents), cells in the culture chambers were exposed to 638 nm laser irradiation with a beam diameter of 5 mm at 600 mW and 1.56 W/cm^2. A medium supplemented with 7% FBS was used in all the experiments.

Additionally. the uptake of FA-AuNPs were analysis also in African green monkey kidney cell line (Vero) as a healthy cell. The cells were cultured in MEM supplemented with 7% v/v FBS and

1% v/v antibiotic. Cell cultures were maintained under standard conditions at 37 °C and a humidified atmosphere containing 5% CO_2 and 95% air.

3.2.4 Crystal violet cell viability assays. The Crystal Violet staining (CVS) is a colorimetric assay based on the growth rate reduction from cell culture plates during cell death. This feature can be used to indirectly assess cell death and determine differences in proliferation rate (Feoktistova, Geserick, & Leverkus, 2016). CVS assay was employed to evaluate cell viability after treatment with AuNPs. After incubation of the cells with different types and concentrations of AuNPs the supernatant was removed and the cells were washed with PBS fixed with methanol for 10 min, stained with crystal violet 0.2% in ethanol 2% for 5 min, and washed 10 times with PBS. Cells were treated with sodium citrate in ethanol 50% for 10 min and absorbance was measured at 550 nm using a Multiskan™ GO's microplate reader. The absorbance values obtained allow to calculate cell viability of treated cells versus control untreated cells.

3.2.5 Flow cytometry measurement. Flow cytometry was performed to differentiate apoptosis from necrotic cell death induced by laser-treated AuNPs and FA-AuNPs. Cells (5.0×10^5 cells per well in 12-well plates) were cultured in MEM supplemented with 7% FBS and incubated at 37 ºC and 5% CO2 for 24 h. AuNPs and FA-AuNPs laser-treated cells were harvested and washed twice in PBS and stained with Muse™ Annexin V and Dead Cell reagent as per manufacturer's instructions (Card, n.d.-a). This assay employs Annexin V to detect PS on the external membrane of apoptotic cells. A dead cell marker (7-AAD) is also used as an indicator of cell membrane structural integrity. Flow cytometry was performed using Muse™ Cell. Data was collected for 10000 gated events using 488 nm light output from an Ar laser as an excitation source.

3.2.6 ROS measurement. After PPT treatment, the ROS levels in cell culture media were determined by incubating HeLa cells with culture media containing AuNPs at 100 μM and exposing the samples to 638 nm laser as previously described. For this assay, cells were seeded in a black 96-well plate to avoid spectral interferences. Subsequently, the laser-treated media were removed, and cells were washed with PBS and incubated with 200 μL of H2DCF (50 μM). The solutions were incubated in the dark for 30 min at 37 °C with 5% CO_2. Then, the fluorescence of the oxidized DCF was measured by using an excitation wavelength of 485 nm and emission of 525 nm during 4 h for each 10 min employing a Fluoroskan^{TM} Microplate Fluorometer. Non-irradiated AuNPs and cells treated with a solution of H_2O_2 400 μM were used as a positive control.

3.2.7 Fluorescence microscopic images. HeLa cells were seeded on coverslips and incubated at 37 ° C with a 5% CO_2 atmosphere for 24 h. Then, they were incubated with different types and concentrations of AuNPs and PPT treatment, the cells were washed with PBS and fixed with 4% formaldehyde in PBS for 1 h at 4 °C. Next, the formaldehyde was removed, and cells were stained blue by using 1.3 mg/ml Hoechst 33343 (nucleic acid stain) for 20 min in the dark at room temperature followed by 3 PBS washes. The cell morphology was observed through a Zeiss vertical microscope (Axio Imager M2) and an AxioCam MRm camera with FireWire (1,4 MP). The image processing was carried out via the Carl Zeiss ZEN 2012 (blue edition) software.

3.2.8 Transmission electron microscopy (TEM) of HeLa cells. The ultrastructure of cells after laser-treated AuNPs were evaluated via TEM. 100 μM AuNPs were added to the medium of HeLa cell and incubated at 37 °C in a 95% air and 5% CO2 atmosphere for 48 hours. After that, the cells were isolated, washed with PBS, and fixed with a mixture of 2% formaldehyde and 2.5% glutaraldehyde in PBS for 1 h at room temperature. The samples were washed four times with PBS for 15 min each time, post-fixed with 1% OsO4 in PBS for 45 min and washed again four times. Subsequently, these samples were treated with 1% uranyl acetate overnight at 4 °C. The samples were progressively dehydrated with absolute ethanol from 30 to 100 % for 10 min for each concentration, and washed twice with 100 % absolute ethanol, each washing lasting 15 min. Then, the pre-inclusion was performed in LRW 1:1 absolute ethanol for 2 h, and then in pure LRW overnight. The cell pellets were embedded in Epon 812 resin using gelatin capsules and polymerized at 50 °C for 48 h, and then detached from the coverslips by successive dips in liquid nitrogen and hot water. Ultrathin sections of 70 nm were obtained in a ultramicrotome (RMC), positioned on FCF -100 Cu and contrasted with 3 % uranyl acetate for 10 min, followed by 2 % lead citrate for 5 min. Finally, the samples were examined on a JEM-200 CX (JEOL) transmission electron microscope at 100 kV and equipped with a digital camera (SIA).

The cellular uptake of AuNPs the samples were also examined by TEM, high-angle annular dark field (HAADF) images were obtained with a FEI Tecnai F30 microscope equipped with a tungsten field emission gun operated at 300 keV.

3.2.9 Statistical analysis. Results are expressed as the average ± standard deviation of three independent experiments. Statistical significance was calculated using ANOVA and multiple comparison analysis averages (Tukey) calculator (GraphPad Software, Inc.). In addition, p-values less than 0.05 (*), 0.01 (**), and 0.001 (***) were considered to be statistically significant.

4 Results and discussion

The results were divided into two sections. In the first section, we report the effect of the different molecular structure of organic solvents in the RMs used as AuNPs reactors in two CTAB-stabilized reversed micellar systems, i.e., toluene/1-butanol/CTAB and *n*-hexane/1-butanol/CTAB. We conduced ^{1}H NMR and FTIR studies to characterize the structural dynamics at interface for both CTAB RMs. The combination of these techniques was applied to gain insight into the structure of RMs to recognize the influence of interface properties in AuNPs synthesis. In the second section, we present the cytotoxicity of AuNPs synthetized via CTAB RMs on HeLa cells with and without laser irradiation and data obtained by different *in vitro* cellular assay performed to display their potential use as photothermal agents.

4.1 Studies in *n*-hexane/1-butanol/CTAB and toluene/1-butanol/CTAB reverse micelles

RMs formed with CTAB generally requires the presence of a cosurfactant, a medium chain alcohol, to form a stable microemulsions and facilitate self-assembly into globular inverse structures over its critical micellar concentration CMC ~ 1 mM up to approximately 0.27 M (Ulmius & Wennerström, 1977; Velegol, Fleming, Biggs, Wanless, & Tilton, 2000) with approximately 1-5.0 nm diameter over a range of W_0 value (Crans, Schoeberl, Gaidamauskas, Baruah, & Roess, 2011; Eastoe et al., 2006b).

The presence of a cosurfactant in quaternary microemulsions provides useful advantages for RM stability and nanoparticle synthesis (Mills, Wilkie, & Britton, 2014). Its presence decreases the interface organization by affecting the compactness of the film and its interface rigidity of the droplets (Curri et al., 2000). Little is known about CTAB RMs microstructures due to their component distribution gives rise to microemulsions of greater complexity, making the determination of size and shape of the aggregates more complicated (Giustini et al., 1996; Mills et al., 2014). The problem of the structure of a quaternary microemulsion is due to when a cosurfactant (i.e., alcohol) is added the dilution is much more complex, since the continuous phase contains alcohol counter to three-component mixtures, where the continuous phase of the droplets is either pure oil or pure water (Langevin, 1988). Accordingly, its characterization by light scattering techniques frequently used to determine the sizes of RMs, seems to exhibit drawbacks (Lang, Mascolo, Zana, & Luisi, 1990). This challenging issue has been extensively addressed and the interface composition characterization has been attained to achieve an understanding of quaternary microemulsions (Pentanol et al., 2003). However, how structural transitions of RMs, produced by varying intrinsic parameters, influence the growth of NPs within the micellar core required a deeper insight. To achieve a comprehensive understanding of the CTAB RMs interface composition dependence on NPs, *n*-hexane/1-butanol/CTAB and toluene/1-butanol/CTAB RMs were selected to be studied as nanoreactors of AuNPs.

Water molecules confined on the reverse micelle experience different environments and hydrogen bonding than bulk water, and have therefore spectral differences (Moilanen, Fenn, Wong, & Fayer, 2009). This was observed by infrared absorption spectrum measured of RMs prepared. CTAB surfactant has a bromide (Br^-) counterions of opposite charge associating with their ammonium charged head groups. Small aqueous droplets that are coated by a layer of surfactant molecules form an interface. Geometrical confinement by an interface may collectively alter the properties of many water molecules, thus anion-bound and water have strong interfacial character and their structural and dynamical properties are different (Onori & Santucci, 1993). An increasing number of works used CTAB as surfactant because of CTAB reverse micellar systems provide a very flexible film, which arises a high exchange dynamic of the micelles (Lopez-quintela, 2003). In addition, interfacial water in cationic CTAB reverse micelles has higher orientational mobility than water in anionic AOT reverse micelles (Dokter, Woutersen, & Bakker, 2007).

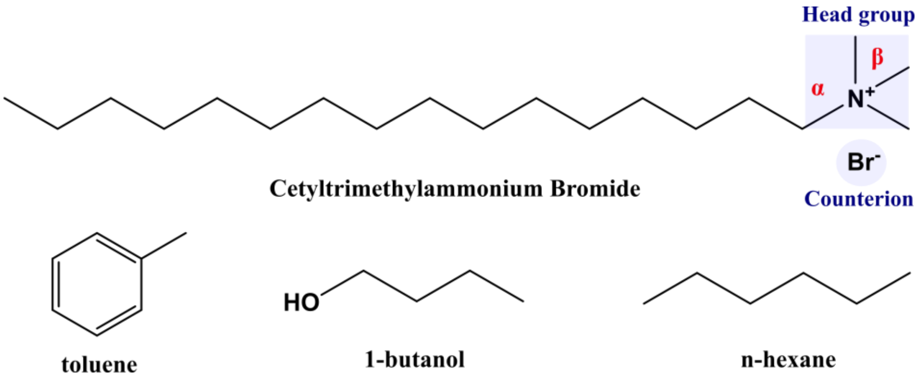

Figure 4. Structures of the cationic surfactant CTAB, cosurfactant 1-butanol and molecules used as continuous phase: n-hexane and toluene.

The OH-stretch absorption spectra of water in CTAB RMs of three different W_0 are shown in *Figure 5*. It is observed the O-H stretching band of water entrapped inside both RMs blue-shifted with respect to the bulk water absorption centered at 3310 cm^{-1}. Increasing the water content from W_0 = 0 to 10, the O-H stretching vibration slightly shifts from 3150 cm^{-1} to higher frequencies of 3170 cm^{-1} in *n*-hexane/1-butanol/CTAB systems reverse micelle, whereas in toluene/1-butanol/CTAB reverse micellar system the O-H stretching band shifts from 3100 cm^{-1} to approach 3070 cm^{-1}. Therefore, a quite remarkable and reproducible change in both reverse micellar systems is observed and decreased with the water content.

The frequency shift in *n*-hexane/1-butanol/CTAB suggests that most of the confined water is bound or trapped near the CTAB $N(CH_3)_3^+$ head groups, which have a very small polarizable electron cloud, increasing the electric field along the direction of the O-H bond. It is because they interact with the oxygen atom of water, as a result of formation a hydration shell of the cationic head group at the micellar interface. Hence, the O-H stretching band exhibits a red-shift of the O-H stretching frequency from the position of bulk water. Studies on hydrogen-bond dynamics in reverse micelles have shown a dependence of red-shift as a directional and not parallel hydrogen bond, which allows a stronger bond with more hydrogen bonds from the surrounding water molecules (Onori & Santucci, 1993; Park, Moilanen, & Fayer, 2008). Therefore, the interfacial water in CTAB reverse micelle system has higher orientational mobility due to the hydration shell around the CTAB head group, as it was observed.

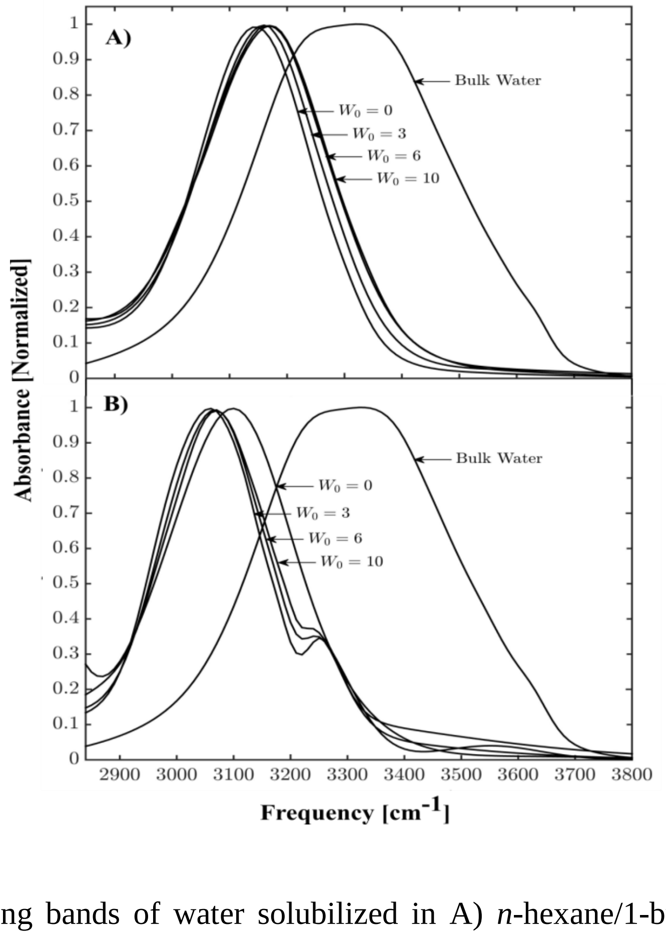

Figure 5. O-H stretching bands of water solubilized in A) *n*-hexane/1-butanol/CTAB and B) toluene/1-butanol/CTAB mixed reverse micelle at different concentration of water content W_0. Bands are normalized to the same height of the maximum band and the vibration absorption of 1-

butanol has been subtracted for each spectrum to avoid spectral overlap with those of the studied water. $W_0 = 0$ does not apply.

In contrast, water confined in toluene/1-butanol/CTAB reverse micellar system showed a different fraction of peak area to *n*-hexane/1-butanol/CTAB system, as well as a second narrowed band around at 3250 cm^{-1} which does not appear at $W_0 = 0$ and has a remarkable increased red-shift. This second band grows at a high frequency compared with the main band and slightly shifts when the micelle water content increases, as Figure 1B shows. This spectrum splitting of the O-H vibration band may result from an interaction of the O-H group with the aromatic π-system of the toluene through the ring, which acts as hydrogen bond acceptors giving rise to the red-shift correlated with the interaction strength between the O-H group and acceptor molecule (Acceptors, Levitt, & Perutz, 1988). A similar O-H stretching band splits into two bands, one of them at the high frequency produced by π-complexes was found by Wayland et al. (1964) in the anisole-phenol system. Two types of frequency shift have also been observed due to the O-H···π interactions in perfluoro-tert-butanol (PFTB) complexes with different aromatic acceptors (Mentel & Luck, 2005). In our case, the splitting of the O-H band, as well as differences in the frequency shift in both RMs system, are due to the different solvent environment at the interface. Nevertheless, we showed that the ability of toluene to interact with O-H groups, which remain associated with the surfactant head group molecules and 1-butanol, is caused by an increase in the surfactant-water contact area at the interface as a result of toluene presence at the interface. Due to the surfactant molecules are higher hydrated, and therefore less packed, they have weaker hydron bound among themselves than water molecules trapped near the head group in *n*-hexane/1-butanol/CTAB, where most of the water molecules in the shell contribute. Thence, the density of water molecules located at the interface of toluene/1-butanol/CTAB is increased. It allows greater penetration of 1-butanol in the interface that makes the interface more fluid. Nevertheless, droplets formed under the aforementioned conditions do not show the same interface rigidity.

Structural properties, location of the organic solvent and surfactant charge of RMs were determined by using ^{1}H NMR spectroscopy below the critical micellar concentration. *Figure 6* displays the ^{1}H NMR spectra collected for *n*-hexane/1-butanol/CTAB and toluene/1-butanol/CTAB at different water content W_0, where it is evident the interaction between cationic surfactant CTAB, continuous phase and water pool. In this RMs system, we focused on the signal associated with the H_α and H_β of CTAB (cf. *Figure 4*), because they are hydrogen atoms closer to the headgroup charge in CTAB. Their location and interaction with other molecules determines the fluidity of the interface and, consequently, the interaction between droplets (Keh & Valeur, 1981).

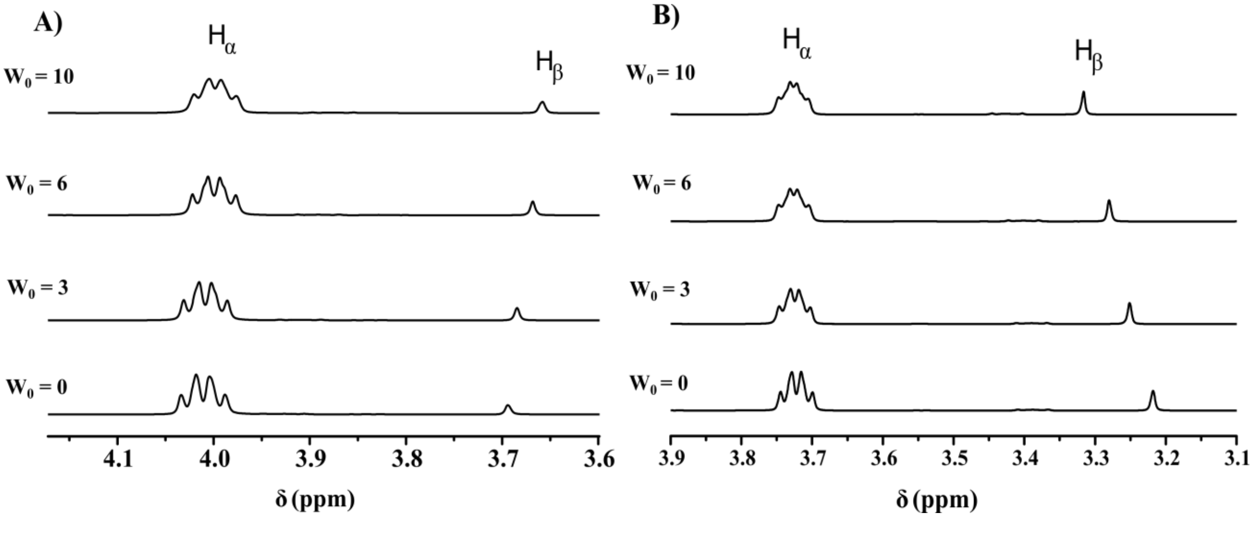

Figure 6. ^{1}H NMR spectra of the CTAB RMs at different water content W_0: A) *n*-hexane/1-butanol/CTAB [CTAB] = 0.1 M, [1-butanol] = 6.5 M; and B) toluene/1-butanol/CTAB [CTAB] = 0.1 M, [1-butanol] = 3.3 M.

Through ^{1}H NMR experiments, downfield shifts were attributed to displacement of protons to more polar environments, *e.g.*, from the micellar core to interfacial water surroundings at the micellar interface, whereas upfield shifts indicate a variation of the proton environment to a non-polar region or better electrostatic screening (Crans, Rithner, Baruah, Gourley, & Levinger, 2006; Kreke, Magid, & Gee, 2002; Lutz-Bueno et al., 2016). Figure 2A shows the ^{1}H NMR spectra of *n*-hexane/1-butanol/CTAB system. H_α and H_β signals shift upfield with increasing W_0 suggest that H_α and H_β CTAB protons are in more hydrophobic and less polar environment deep in the interface layer of the micelle. It may also explain that the environment of the headgroup charge of the CTAB be confinement, which indicates that the hexane with a higher molecular bulkiness probably cannot penetrate the surfactant tails so efficiently, leading a lower interaction between surfactant and 1-butanol, thereby a more compact interface (Chandler, 2005). In turn, it increases the rigidity in the RMs interface, compared to a dynamic interface layer of a reverse micelle that would contain penetrating cosurfactant and water (Gaidamauskas, Cleaver, Chatterjee, & Crans, 2010).

^{1}H NMR spectra of toluene/1-butanol/CTAB display a completely different chemical shift profile than observed in *n*-hexane/1-butanol/CTAB system, both H_α and H_β proton signals shift to downfield. The H_β proton environment in CTAB is probably hydrophilic and more polar considering the further downfield shifts. Hence, it can be established that protons are penetrating deeper into the micellar interface and producing a stronger interaction with the entrapped water inside CTAB RMs. This behavior has been attributed to solvents with a lower molecular bulkiness, such as toluene, that can penetrate between surfactant tails (Salabat, Eastoe, Mutch, & Tabor, 2008). Therefore, the toluene (V_M = 106.2 cm^3 mol^{-1}) can penetrate the CTAB RM interface more easily than *n*-hexane (V_M = 131.6 cm^3 mol^{-1}). Consequently, when penetration of the oil into the interface was increased, there was an increase in the separation between CTAB molecules and, thereby, a decrease in the rigidity of the CTAB film, which facilitated the penetration of water molecules into the interface. It strongly suggests that 1-butanol is solubilized essentially in the interfacial film. A similar preferential penetration by an aromatic solvent in AOT (García-Río et al., 2006; González-Blanco, Rodríguez, & Velázquez, 2002) and Triton X-100 microemulsions has been observed (Zhu, Wu, & Schelly, 1992).

As expected, the interfacial polarity and the water-CTAB head group interaction depend dramatically on the external non-polar solvent composition, and must be relevant because the mass transfer is not possible unless the interface is disrupted (García-Río et al., 2006). It has also been generally observed that an interdroplet attractive interaction of RMs can be "switched on" (increased) and "switched off" (decreased) by applying mixtures of solvents, which are denominated as *"good"* and *"bad"* solvents depending on whether they decrease or increase the strength of interactions between droplets, respectively (Federico M. Agazzi, R. Dario Falcone, Juana J. Silber, 2011; Hollamby et al., 2008; Myakonkaya et al., 2009). In the same way, it is observed that the magnitude of the droplet-droplet interactions in *n*-hexane/1-butanol/CTAB RMs is greater than that of those in toluene/1-butanol/CTAB. It is because of the attractive interaction between droplets increased, favoring interdroplet interactions and leading to a higher tendency to aggregate and also results in more stable RMs (Salabat et al., 2008). Moreover, this fact could be correlated with the surfactant packing and, therefore, have an effect on the RMs droplet sizes, as observed above (Gutierrez et al., 2014; Q. Li, Li, Wu, & Zhou, 2000).

From the two RM systems studied, the effects of micelles on the continuous phase produced clearly different micellar environments, and these results evidence how the penetration of surfactant into interface varied with an organic solvent. This is a relevant fact to take in account when they are used as a nanoreactor, because the van der Waals interactions with CTAB head ensure the formation of a more compact and stable interfacial film, which protects nanoparticles from aggregation and modulates a nonuniform growth (Drofenik, 2005). It is important to recognize that these microemulsions are not real templates, the mechanism by RMs that acts during nanoparticles synthesis is based on interactions between droplets via Brownian motion, in which the droplets collide and form transient dimers or encounter pairs in a diffusion-controlled process (Fletcher, Howe, & Robinson, 1987). The intermicellar material exchange is only possible if the fusion process is followed by the formation of a channel opened through the surfactant bilayer between droplets (M. A. López-Quintela, Rivas, Blanco, & Tojo, 2006). Therefore, it depends strongly on the film flexibility. In this way, to determine how interdroplet interaction owing to the type of external solvent influences the AuNPs synthesis, the following section presents the AuNPs synthesis using toluene/1-butanol/CTAB and *n*-hexane/1-butanol/CTAB RM systems at $W_0 = 6$.

4.2 CTAB reverse micelles as nanoreactors

Reverse micelles systems are an attractive alternative for controlling nanoparticles synthesis due to their tunability of the synthesis parameters. In these systems, nanoparticles are formed in chemical reactions which take place in confined environments under control at the interface, where mass transfer through droplet-droplet exchange occurs. In this sense, the confinement effect and interfacial properties play an important role in explaining that chemical reaction. The concentration of the precursors, W_0 value, cosurfactant as well as presence of several additives were specifically changed for tuning the reaction rates, mostly in AOT RMs (Bagwe & Khilar, 1997; García-Río et al., 2006; Hait, Sanyal, & Moulik, 2002; Lopez-quintela, 2003; M. A. López-Quintela et al., 2004).

There is an increasing number of works employing CTAB as surfactant because it provides a very flexible film and gives rise to a high exchange dynamic of the micelles. This is possible due to it possess a great water solubilization capacity compared to AOT RMs, as remarked above. Although the use of CTAB RMs for the preparation of nanoparticles has been increased, most have focused on studying their microstructure and dynamic physical properties (Mills et al., 2014; Pentanol et al., 2003). Consequently, a very few CTAB reverse micellar interface studies have been conducted to report the effect of changing the composition of the organic solvent in the design of CTAB RMs to be used as nanoreactors for AuNPs synthesis. Therefore, we deepened in the intedroplet interaction by evaluating the effect of the nucleation and growth processes in two CTAB RMs systems.

Considering the chemical shifts observed by ^{1}H NMR and FTIR spectroscopy, which manifest two different CTAB RMs interface environment, the influence of intermicellar exchange by varying the organic solvent by using *n*-hexane and toluene as continuous phase was studied. Figure 3 compares the absorption spectra as a reaction time function of AuNPs formed in two different reverse micelles at $W_0 = 6$. The plasmon absorption peak shifts toward longer wavelengths in toluene than in hexane. It is noteworthy that the magnitude of these shifts is quite different in both reversed micellar systems. Thus, it was decided to evaluate AuNPs properties at 5 s, 10 s, and 30 s of reaction time with L-cysteine (L-Cys), enhancing their stability, controlling their size and characterizing the growth of nanoparticles, since the aggregation and dispersion properties of colloidal particles control their potential applications. In the *n*-hexane/1-butanol/CTAB RMs system, a progressive red-shift is observed from $\lambda_{max} = 571$ nm at 5 s to $\lambda_{max} = 614$ nm at 30 s (cf. Figure 7A.). The high intensity and sharp profile of the localized surface plasmon resonance

(LSPR) peaks suggest the small size of the particles formed in comparison with the synthesized AuNPs in toluene/1-butanol/CTAB. Herein, LSPR values show less intense and largest red-shifted from λ_{max} = 586 nm at 5 s to λ_{max} = 653 nm at 30 s (cf. Figure 7B). Similar red-shift has been observed in the measured optical spectra of AuNPs and was attributed to the effect of electromagnetic delay in larger nanoparticles (P. Jain, Lee, & El-Sayed, 2006).

Moreover, it is known that the development of the broad peak at long wavelength come from the coupling of the SPR of two adjacent nanoparticles, when the interparticle distance in the aggregated nanoparticles decreases to less than about the average diameter of nanoparticles, and is an indication of the anisotropic optical properties of the AuNPs (Jana, Gearheart, Obare, & Murphy, 2002). Thus, the evolution of optical absorption spectra of AuNPs suggests an increase of size as a function of the reaction time. Whereas, the features of the LSPR obtained in the two RM systems is attributed to a variation in nanoparticle morphology. To illustrate the effect of the RMs water pool size on final properties of AuNPs, *Appendix A* and *B* present the absorption spectra of AuNPs synthesized by *n*-hexane /1-butanol/CTAB and toluene/1 butanol/CTAB RMs at W_0 = 3 and W_0 = 10. These spectra showed similar LSPR features than W_0 = 6. However, AuNPs obtained at W_0 = 6 for two RM systems were chosen to be studied due to their higher stability over time.

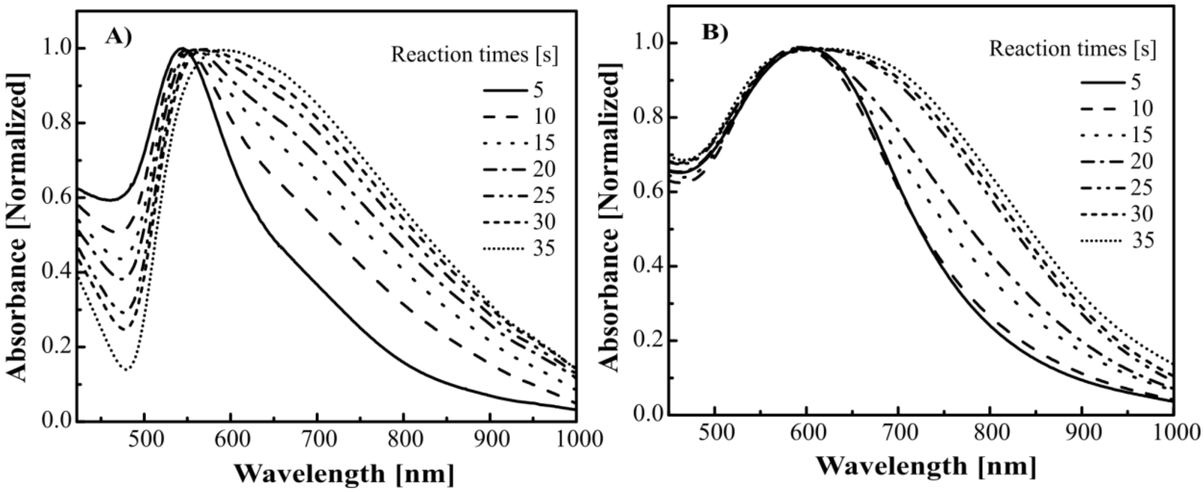

Figure 7. Absorption spectra of AuNPs synthesized by A) *n*-hexane /1-butanol/CTAB RMs at W_0 = 6, [CTAB] = 0.1 M, [1-butanol] = 6.5 M and B) toluene/1 butanol/CTAB RMs at W_0 = 6, [CTAB] = 0.1 M, [1-butanol] = 3.3 M as a function of reaction time. An empty CTAB RM solution was used as a blank in both cases.

TEM micrographs for AuNPs synthesized in the *n*-hexane/1-butanol/CTAB RMs and stabilized with L-Cys (0.03 M) at 5 s, 10 s, and 30 s of the reaction time confirmed the formation of small spherically (or ellipsoidal shapes), as Figure 8A displays. It is noticed that a significant agglomerate of AuNPs was formed and, especially for sample stabilized at 30 s of the reaction time, which indicated a time evolution of the particles self-aggregation. This can be due to the formation of bridges between the nanoparticles and induction aggregation. Therefore, the induced AuNP aggregation by addition of L-Cys was attributed to the formation of zwitterionic networks involving interaction of the deprotonated carboxylate ($-COO^-$) and protonated amine ($-NH_3^+$) groups between AuNPs-bound to L-Cys, with the opposite groups of L-Cys capped on neighboring particles, consistent with studies conducted using FTIR spectroscopy and other techniques (Acres, Feyer, Tsud, Carlino, & Prince, 2014; Mocanu et al., 2009; Sudeep, Joseph, & Thomas, 2005). Figure 8B shows the corresponding histogram providing the size distribution of AuNPs, indicating a normal distribution with a progressive increment of size from 9 nm to 14 nm. These measures supported the phenomenon of color change resulting from the increase in average particle size and, hence, of aggregation (Figure 8C and 8D).

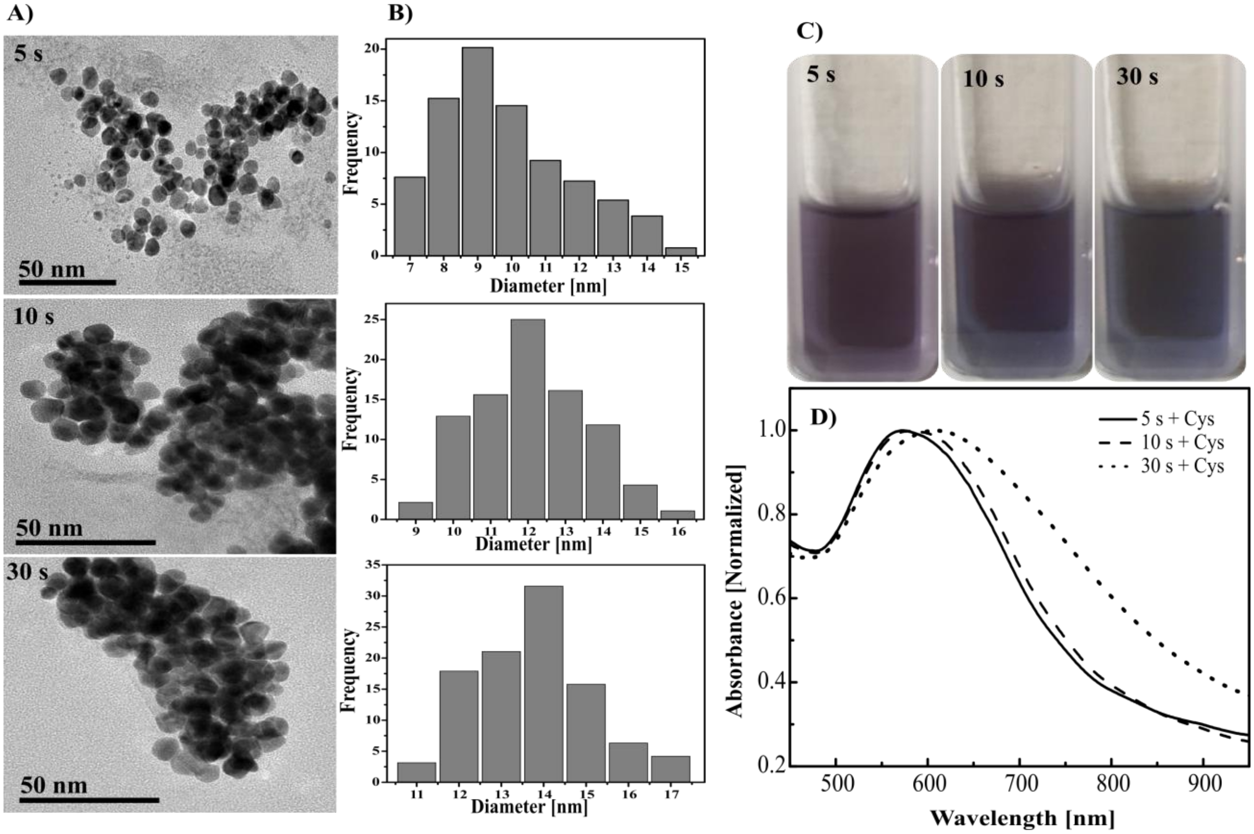

Figure 8. A) TEM micrographs. B) Size distribution. C) Digital photographs of AuNPs in reverse micellar media. D) Absorption spectra of AuNPs synthesized by *n*-hexane/1-butanol/CTAB RMs at $W_0 = 6$, [CTAB] = 0.1 M, [1-butanol] = 6.5 M after L-Cysteine stabilization (0.03 M) at 5 s, 10 s and 30 s of the reaction time. Data for the histogram were collected from 100 randomly picked particles.

The monodisperse and smaller particles observed for each TEM micrograph and size distribution plot in Figures 8A and 8B indicate that the particle growth rate is slow. It is due to hexane has a larger molecular bulkiness and the penetration of its surfactant tails is impeded. Also, the interaction with the head group is not efficient. Therefore, these facts lead an increase in the surfactant curvature and rigidity. The RMs interaction potential becomes more attractive when increasing the partial molar bulkiness of the oil, consistent with a precise analysis of the thermodynamically behavior of microemulsion (Lemaire, Bothorel, & Roux, 1983). As it is difficult for larger solvent molecule to penetrate the interface, the surfactant has a great network attraction that makes it optimally packaged due to changes in entropy of conformation. This process induces a removing of continuous phase molecules and produces a large overlap. The CTAB interface composition favors the interchange of precursors leading a fast nucleation process, thus the rate of material exchange among micelles is increased in these RMs. It was evidenced by ^{1}H NMR spectroscopy as an upfield shift of the protons of the surfactant head group given its deficient penetration into the polar core. Similar spherical and highly monodispersed AuNPs were found in *n*-heptane/AOT/water RMs by Gutierrez et al. (2014). They reported a fast nucleation process according to the fact that the droplet–droplet interactions are favored and the rate of material exchange among the micelles is increased in these RMs. Indeed, their results are consistent with the classical nucleation theory that happens when the high surface-to-volume ratio of the nucleus is formed as a result of homogeneous nucleation, which is originated a high thermodynamic energy barrier. This energy barrier plays an important role in the synthesis of uniformly sized nanoparticles due to it suppresses the random formation of particles under high supersaturation (J. Lee, Yang, Kwon, & Hyeon, 2016; Pileni, 2006; Soon Gu Kwon,† Yuanzhe Piao,† Jongnam Park,† Subramanian Angappane,‡ Younghun Jo,§ Nong-Moon Hwang,| Je-Geun Park, 2003).

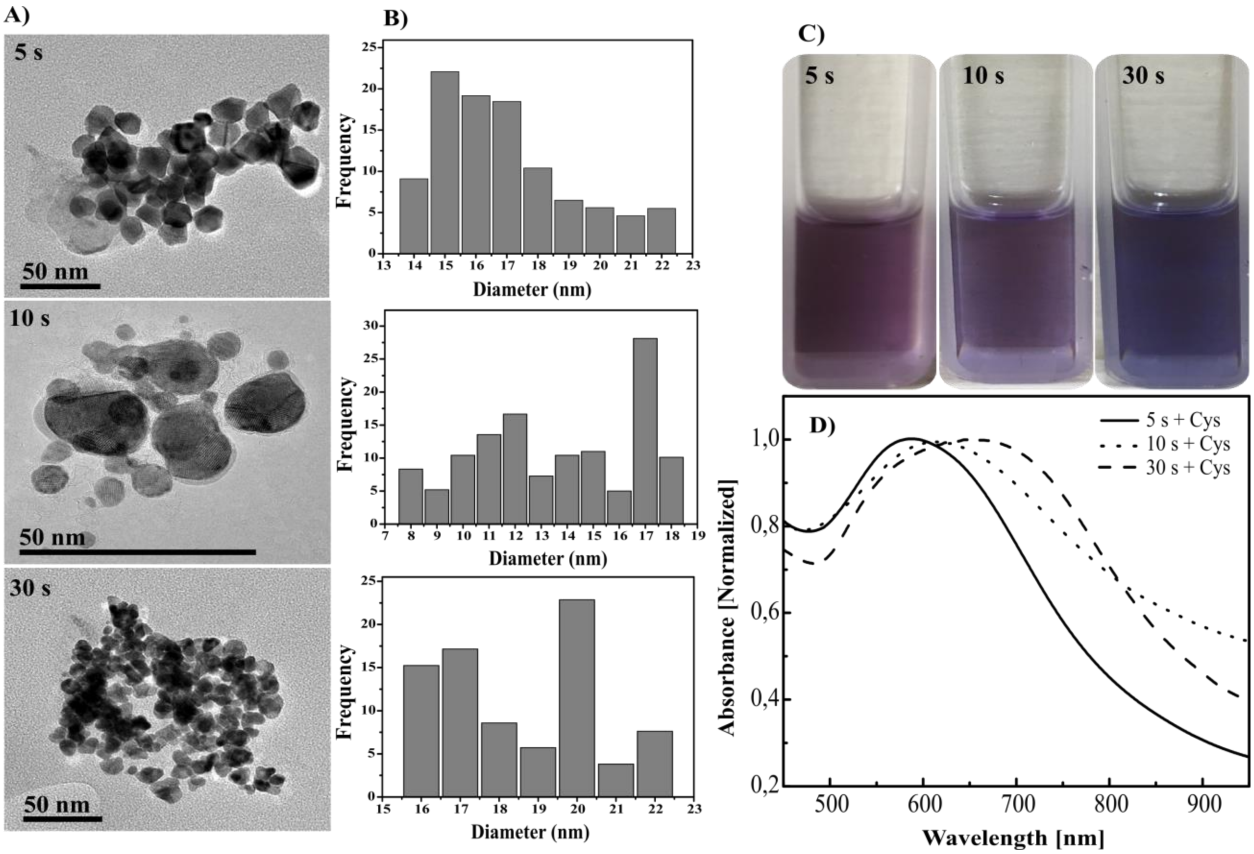

Figure 9. A) TEM micrographs. B) Size distribution. C) Digital photographs of AuNPs in reverse micellar media. D) Absorption spectra of AuNPs synthesized by toluene/1-butanol/CTAB RMs at $W_0 = 6$, [CTAB] = 0.1 M, [1-butanol] = 3.3 M after L-Cysteine stabilization (0.03 M) at 5 s, 10 s and 30 s of the reaction time. Data for the histogram were collected from 100 randomly picked particles.

For comparative purposes, AuNPs particles synthesized in the toluene/1-butanol/CTAB RMs are anisotropic and not all particles present identical shape, see Figure 9A. In this case, the particles exhibit a more complex network, i.e., spheres and hexagons coexist with triangles, but some particles also exhibit a small spherical polycrystal shape into the aggregated. Figure 9B shows histograms indicating a relatively high degree of polydispersion and broad distribution, most of the nanoparticles have a progressive increment of size from 15 nm to 20 nm. It is noticeable that the crystallization renders various assembly and aggregation behaviors, which lead to an anisotropic crystal growth further evidenced by the noticeable color change observed in Figure 9C and 9D. It is consistent with the description for a nonclassical crystallization as a pathway according to Lee et al. in (2016). They studied the formation of diverse intermediate structures between atoms and crystalline solids, including nanoclusters and nanoparticles, by changing the traditional view of crystallization instead of the direct assembly of atoms into crystalline lattice. In effect, the intermediate structures in nonclassical crystallization show various assembly and aggregation of nanoparticles. From these data, one can expect that the RMs interface properties regime is a key parameter for controlling the nanocrystal growth.

The origin of differences in crystallization behaviors of AuNPs obtained in both RM systems is explained in terms of solvent molecular structure and their ability to penetrate the surfactant tail region. Between the two systems, the size and polydispersity of the synthesized AuNPs increased when toluene was used as the organic phase. These results corroborated the fact that, in the case of toluene, the molecules penetrate between surfactant tails leading an efficiently association of 1-butanol into the interface and, therefore, its curvature is relatively gentle i.e., the interface is fluid due to the small packing of the head groups. As the difference between the composition of the interface and the continuous phase decreases the net intermicellar attraction is reduced (J. S. Huang et al., 1984). When there is a weakly intermicellar overlap, the number of successful collisions leading to exchange of matter is less and, thus, higher growth rates, i.e., diffusive transport cannot satisfy the demand at the growing surface (Angelomé et al., 2012). Hence, a smaller number of nuclei can be produced, and the particle size is expected to be as large as polydisperse as was observed to AuNPs synthesized by toluene/1-butanol/CTAB.

Structural variances can contribute to the nonclassical nucleation pathway as started above. The formation of intermediate structures with a low surface and bulk-free energy reveals the presence of local minima in the energy landscape, which provides an alternative pathway to lower the energy barrier for nucleation. Then it can take place at a level of supersaturation lower than the estimated by the classical nucleation theory (J. Lee et al., 2016). As a result, the nuclei formed via nonclassical nucleation are thermodynamically stabilized by their strong tendency for minimizing their surface energy under ripening by increasing their size, as Oswald's step rule conjectured (Van Santen, 1984). Previous works have demonstrated that CTAB and their chloride counterpart (CTAC) have allowed the preparation of AuNPs with highly anisotropic and unusual shapes, such as stars, nanoprisms, nanorods (Angelomé et al., 2012; Gómez-Graña et al., 2012; Ha, Koo, & Chung, 2007) and even novel nanostructures, i.e., rhombic dodecahedra or bipyramids (Personick et al., 2011). The reason for such different nanocrystal shapes obtained with CTAB and CTAC is attributed to the ability of bromide and chloride ions to chemisorbed on the AuNPs surfaces, and the control of growth rate of the nuclei and the morphology (Filankembo, Giorgio, Lisiecki, & Pileni, 2003), via adsorption on specific nanocrystal facets (Pileni, 2007; Rai, Singh, Ahmad, & Sastry, 2006). In this way, it is particularly noteworthy that the interfacial polarity and the high hydration of CTAB head group found in toluene/1-butanol/CTAB produce free (Br^-) ions that can be introduced into reactive media involved in anisotropic effect, due to their adsorption affinity on gold surfaces. Whereas, in *n*-hexane/1-butanol/CTAB, the counterion is located at the interface near the CTAB head group, as it was confirmed above with FTIR. This fact is further evidence of how changing the composition of the RMs interface plays a significant role in the nanocrystal growth. Similar results for gold nanoparticles were also observed in water/BHDC/toluene RMs by Blach and Martínez (Diana Blach & Martínez, 2017). They showed polycrystalline lattice without preferences for the attachment on AuNPs due to the availability of (Cl^-) ions at the interface inducing anisotropy and polycrystallinity.

Spherical and anisotropic AuNPs, each one of two different sizes (9 and 14 nm, 15 and 20 nm, respectively), synthesized via the former approach were chosen to be tested as candidate photothermal agents in the well-known human epithelial cervical cancer cell line (HeLa). Furthermore, these AuNPs were conjugated with FA to evaluate their biocompatibility and target cancerous cells. For this purpose, the surface physicochemical properties of these NPs were characterized to carry out the in vitro assays. Subsequently. the influence of the size, shape and surface conjugation on cytotoxicity and photothermal effect of AuNPs to HeLa cells were elucidated.

4.3 Spectral characterization of FA-AuNPs

The surface charge of FA-conjugated AuNPs were followed by zeta potential (ζ) measurement. It is important to note that ζ measurements were done in aqueous media at a pH about 7.0. Results are summarized in *Figure 10*. It is observed an inversion of the positively charged surface of spherical AuNPs of 9 and 14 nm (i.e., ζ + 29.9/62.3 mV), and after conjugation with FA (i.e., ζ – 18.0/28.9 mV), respectively. For the case of anisotropic AuNPs of 15 and 20 nm it showed the same inversion of zeta potential values; from (ζ + 28.3/30.4 mV) to (ζ – 15.0/21.2 mV). Such a behavior can be explained based on the ionization process of FA at pH 7,0; the pKa of carboxylic groups of the glutamic acid is around pH = 3-7. Therefore, these carboxylic groups along glutamic acid are ionized (cf. the inset in *Figure 10*). Over this pH range it is also negatively pteridine ring stated to form. Then, either carboxylic or amine groups of the anionic FA allow the electrostatic association with the surface of AuNPs leading to a reversal surface charge of AuNPs from positive values, to negative values, for AuNPs-FA. Nevertheless, surface-enhanced Raman scattering (SERS) spectra and density functional theory (DFT) calculations indicated that the interaction of FA with AuNPs occurred primarily through the nitrogen atoms, from their pteridine ring (Castillo, Rindzevicius, Rozo, & Boisen, 2015). Besides, it was shown that N–Au bonding interaction might be formed in this system (Di Felice & Selloni, 2004). It is worth noting that this FA conjugation onto AuNPs preserves the NPs negatively charged and, provides colloidal stability (X. Huang et al., 2008).

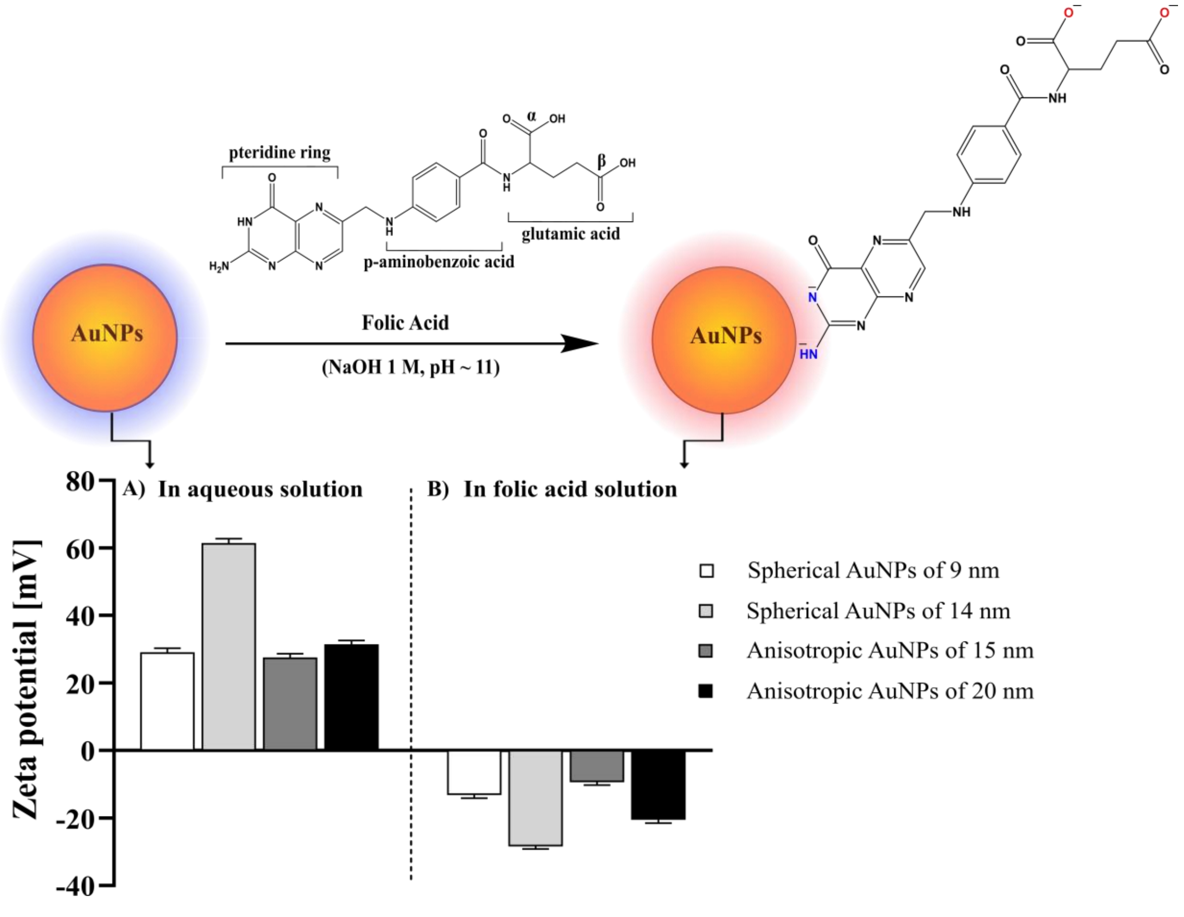

Figure 10. Zeta potential distribution of A) AuNPs and B) FA-AuNPs. Error bars represent standard error of mean with n = 3 per group. The inset shows a schema depicting the AuNPs conjugation using FA.

Additionally, FTIR analysis was carried out to provide information about the functional groups involved in the conjugation process of FA to AuNPs. As *Figure 11A* shows, the bands that appear at 1688 cm^{-1} and 1602 cm^{-1} correspond to (-COO^{-}) symmetric stretch mode and (-NH) bending mode of FA, respectively. The shift from characteristic C=O stretching vibration of 1964 cm^{-1} to 1688 cm^{-1} belongs to the carboxyl change into carboxylate group. Moreover, the bands between 1481 and 1451 cm^{-1} are attributed to the characteristic absorption band of the phenyl and pterin ring (Zhang, Rana, Srivastava, & Misra, 2008). The characteristic IR absorption bands of FA are also observed in the spectrum of FA modified AuNPs. A simultaneous shifted to a higher frequency is observed at a reduced intensity due to the small concentration of FA on the AuNPs surface. These spectral differences from the pure FA indicate structural changes in which -COO^{-} groups of the glutamic acid and -N-terminal groups of the pterin ring are involved in the interaction of FA with AuNPs.

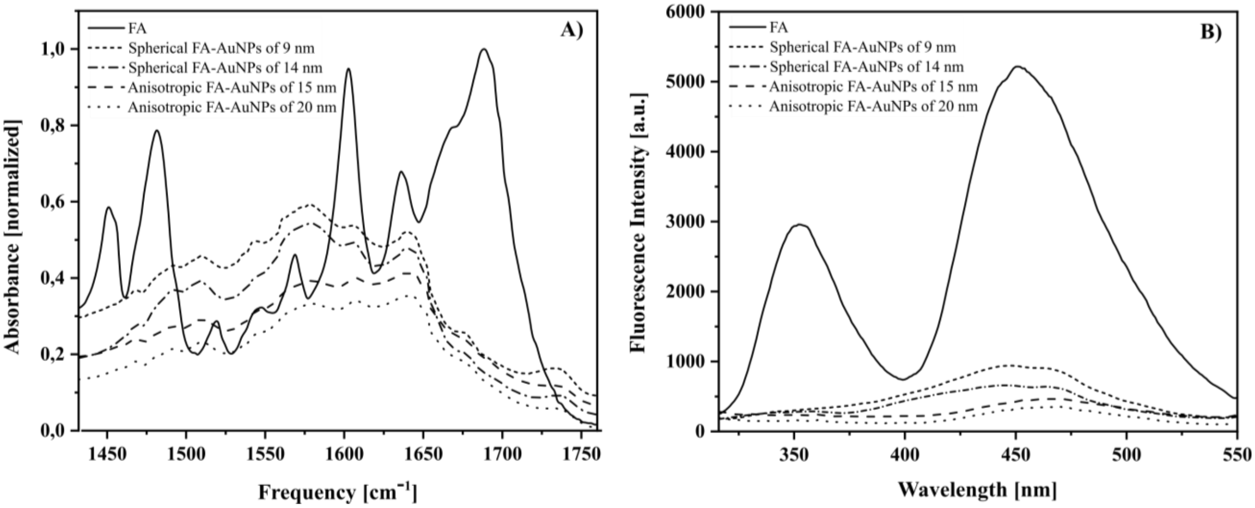

Figure 11. A) FTIR spectrum and B) fluorescence emission spectra of FA and the FA-AuNPs at [Folic acid] = 1 × 10^{-3} M, [Au] = ~ 400 µM in water. The excitation wavelength used was 364 nm.

Metal surfaces can interact with negatively charged carboxyl and amine groups obtained by deprotonation of donor groups as carboxyl acids and primary aromatic amines (Neouze & Schubert, 2008). This is consistent with the acid dissociation constant (pKa) of FA, which has been determined by a capillary electrophoresis technique to acquire four pKa values (i.e., 2.38, 3.46, 4.98, and 8.08) as overall equilibrium constants. pK_1, pK_2, and pK_3 constant values are related to deprotonation sequences α-COOH, β-COOH, and NH_2, respectively. The pK_4 value of folic acid was assigned to the NH/CO fragment of the pteridine ring (cf. the inset in *Figure 10*) (Szakács & Noszál, 2006). Accordingly, the deprotonated folic species started to form in acidic conditions (pH from 2 to 5.5) and wholly formed in neutral and alkaline conditions (pH from 5.5 to 9.5) (Fazary, 2013). FTIR studies, as well as theoretical calculation, revealed that the coordination of terminal amine and carboxyl groups is based on a combination of electrostatic and hydrophobic interactions of the ligand and the NP surface, which are obtained by deprotonation of this donor groups (Neouze & Schubert, 2008). Hydrophobic interactions are due to attraction between hydrophobic parts of the ligand and the metal surface that results in the formation of a non-covalent bond. Concomitantly, an ionic interaction is formed between negatively and positively charged groups and the surface of particles (Rayavarapu et al., 2007).

Molecular chromophores as some biomolecules adsorbed on the surface of the NPs, usually experience quenching of their fluorescence. Furthermore, the fluorescence background revealed that the AuNPs quenched excited states of the chromophores because they can also participate in an electron-transfer process and decrease the probability for radiative transitions (Ipe, George Thomas, Barazzouk, Hotchandani, & Kamat, 2002; Schneider et al., 2006). Therefore, fluorescence emission spectroscopy was performed to study the interaction of FA with AuNPs at the molecular level. *Figure 11B* shows the emission spectra of FA and FA-AuNPs suspended in water. The FA exhibit two broad emission band: a weaker band centered around 352 nm and a stronger band centered around 451 nm.

In contrast, AuNPs-AF only show a prominence of peak II over peak I at a reduced intensity. However, the fluorescence signals are significantly quenched by the AuNPs. IT Is important to note that the decrease in emission intensity is proportional to the reduction in the size of the AuNPs. These results are consistent with those previously reported by Paramanik et al. (2007). They found that quenching of fluorescence of the Safranine T dye decreased with the decrease in the size of the NPs of AgCl. Aforesaid a behavior is related with successful conjugation of the FA to the AuNP surface due to only efficient quenching of fluorescence is possible in the concentration range in which the available gold surface is not completely saturated (Montalti, Prodi, Zaccheroni, & Battistini, 2004). Hence, it is possible to confirm that the FA concentration used was indicated to produce an efficient conjugation of FA to AuNPs.

4.4 Cytotoxicity assay of AuNPs and FA-AuNPs

To evaluate the possible cytotoxic effects of AuNPs and FA-AuNPs, we used the crystal violet method in the presence of different concentrations of the nanoparticles. Crystal Violet stain no-fragmented membrane cells, so it can be used as indicative of cellular viability (Feoktistova et al., 2016). *Figure 12* shows the cytotoxicity of spherical and anisotropic AuNPs and FA-AuNPs on HeLa cell. The viability of non-conjugated spherical and anisotropic AuNPs treated cells were similar across different concentration. Generally, the viability of cells was not affected even at high concentration of 100 μM. These data highlight that the cytotoxicity effect of AuNPs was not dependent on size or shape. A Similar results were reported by Pan et al. in (2007), they demonstrated the dependence of the toxicity of AuNPs with their size in the range from 0.8 to 15 nm. The AuNPs of 15 nm have been found to be 60 times less toxic than 1.4-nm AuNPs. It has also been shown that large AuNPs (10 or 16 nm) only penetrate through the cell membrane and are found only in the cytoplasm, whereas AuNPs between 2-6 nm effectively enter the cell nucleus, which results in higher cytotoxicity and immunological response (Huo et al., 2014; Yen, Hsu, & Tsai, 2009). In this sense and taken together, these findings suggest that spherical and anisotropic AuNPs with a size range of 9, 14, 15, and 20 nm are not inherently toxic to HeLa cells.

On the other hand, when HeLa cells were incubated with spherical and anisotropic FA-AuNPs, cell viability significate increased compared to control and a concentration-dependent cell response was also observed. At a concentration of 10 μM, cell viability increased to 116% in treatment with spherical FA-AuNPs of 9 nm. At 50 μM, the viability increased to 119% and 115% with spherical and anisotropic FA-AuNPs of 9 and 20 nm. Finally, at 100 μM the viability increased to 126%, 117%, 113% and 119% for treatments with spherical (of 9 and 14 nm) and anisotropic (of 15 and 20 nm) FA-AuNPs, respectively. Considering that non-conjugated AuNPs do not acute cytotoxicity, these results suggest strong activation of the HeLa cells in which FA promote cell proliferation (G. Li et al., 2009). This behavior evidences the high biocompatibility of FA-AuNPs as was previously observed (Liu, Huang, Zhang, Ren, & Wilson, 2010). Furthermore, this cellular response supposes an internalization via receptor mediated endocytosis facilitated by the folate receptor (FR) overexpressed in HeLa Cell (Parker et al., 2005). Additionally, comparing particles sizes with the same shape, a significant size-dependent effect is not noticed, whereas comparing anisotropic AF-AuNPs to spherical AF-AuNPs, an increase in viability is observed with the latter. The intracellular uptake can be significantly affected by the geometrical parameters as well as the uniform distribution of ligand molecules on the particle surface (Decuzzi & Ferrari, 2008). Therefore, spherical AuNPs with a very high aspect ratio favors FA-conjugation as was observed with the zeta potential measurements and thus allow better cellular recognition.

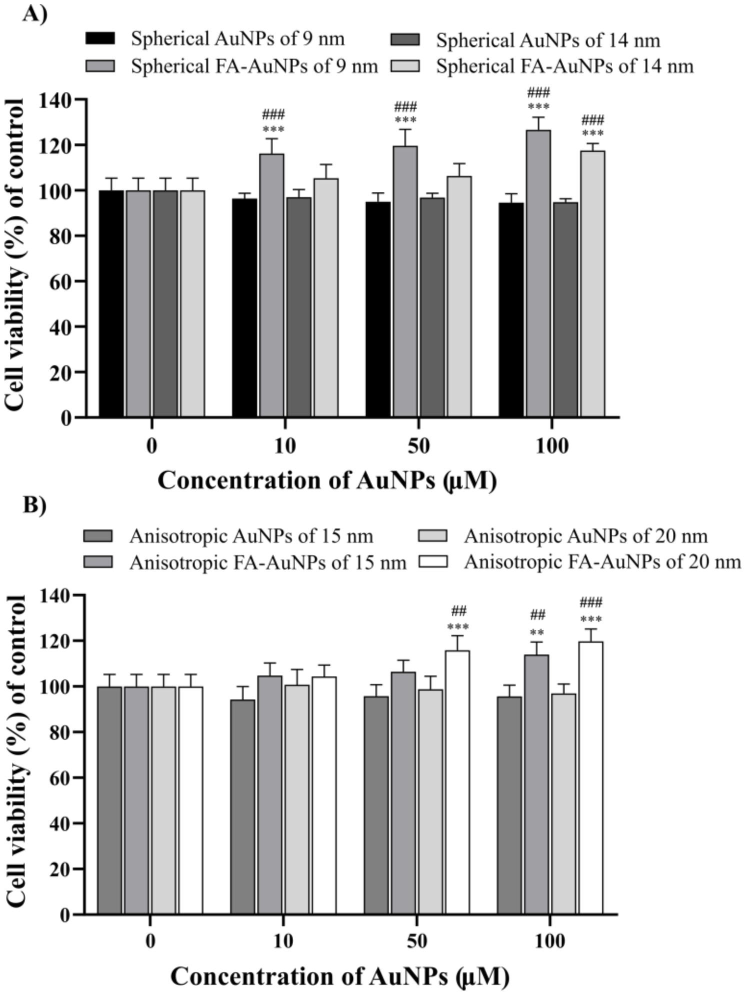

Figure 12. Cell viability assay of HeLa cells after 4 h of treatment with various concentrations of A) spherical and B) anisotropic AuNPs and FA-AuNPs. The values represent the mean ± standard deviation of three independent experiments. *denote significant difference with respect to the control: $*p < 0.05$, $**p < 0.01$, $***p < 0.001$ and $^{\#}$denote significant difference between AuNPs and FA-AuNPs: $^{\#}p < 0.05$, $^{\#\#}p < 0.01$, $^{\#\#\#}p < 0.001$.

4.5 PPT using spherical and anisotropic AuNPs

A diverse variety of AuNPs have been explored for use in therapy and imaging applications (Nazir, Hussain, Ayub, Rashid, & MacRobert, 2014). The key features to consider when selecting a particle for photothermal treatment are the wavelength of maximal absorption and the size of the particle (Khlebtsov, Zharov, Melnikov, Tuchin, & Khlebtsov, 2006). In this section, the effect of the size and shape of AuNPs on the photothermal response in HeLa cells was conducted. HeLa cells were incubated with 10, 50, 100 μM of AuNPs for 4 h and then irradiated with laser of 638 nm and 600 mW for 5 min. Each sample was illuminated at a constant fluence rate of 1,56 W/cm^2. Light control experiments without NPs under 5 min light irradiation demonstrated that 96% of the cells were viable, as *Figure 13* shows. Moreover, negligible differences in cytotoxicity were observed between light control experiments and control experiment, indicating that the cell viability were not affected by the laser conditions (cf. *Appendix C*).

Figure 13 shows the cytotoxic effect of spherical and anisotropic AuNPs after irradiation; it can be observed a concentration-dependent cell response across the sizes and shapes. At high concentration of 100 μM, the viability dropped to 82% using spherical AuNP of 9 nm, which is significantly lower than viability around 65% obtained with spherical AuNPs of 14 nm. Likewise, at the same concentration, anisotropic AuNPs of 15 and 20 nm diminished significantly cells viability to 76% and 60%, respectively, compared to the light control. When comparing the cellular response with AuNPs-irradiated treatment, it is possible to observe that the cell viability decreases when the nanoparticle size increases and that the treatment with anisotropic AuNPs of 20 nm have the lowest cell viability.

The trend observed is consistent with the fact the laser light at 638 nm is directly absorbed by the AuNPs through surface plasmon absorption. The spherical AuNPs of 14 nm show the SPR band around 563 nm, whereas anisotropic AuNP of 19 nm exhibit a broad absorption band centered at 656 nm that is overlapped by laser light wavelength (cf. *Appendix D*). This strong absorption of laser light directly induces temperature rises of the cells around the AuNPs and thus renders cell damage. The photothermal response of the AuNPs solutions during 630 nm laser irradiation was measured in the cell culture media (MEM). As shown in *Appendix E*, the suspensions of AuNPs exhibited a rapid size-dependent temperature increase. Upon increasing the exposure time to 10 min, the photothermal response of spherical AuNPs of 9 nm was found to reach a maximum increase of 3.0 ± 1 °C, whereas spherical AuNPs of 14 nm increased the temperature by over 4.4 ± 1 °C. The anisotropic AuNPs of 15 nm reached a maximum increase of 4.0 ± 1 °C, whereas anisotropic AuNPs of 19 nm reached an increase of 5.3 ± 1 °C. In comparison, the media without NPs showed a minimal photothermal response, only reaching an increment of ~ 1 °C. Nonetheless, among large spherical and anisotropic, the latter shows a higher photothermal efficiency indicating a substantial heating effect of AuNPs on cytotoxicity. All four AuNPs solutions displayed a photothermal response and the differences in temperature are again related to the overlap between the AuNPs LSPR and the wavelength of laser source. The enhance photothermal response of large anisotropic AuNPs, relative to the small spherical and anisotropic AuNPs, suggests the potential of the anisotropic AuNPs of 20 nm as effective PPT agents.

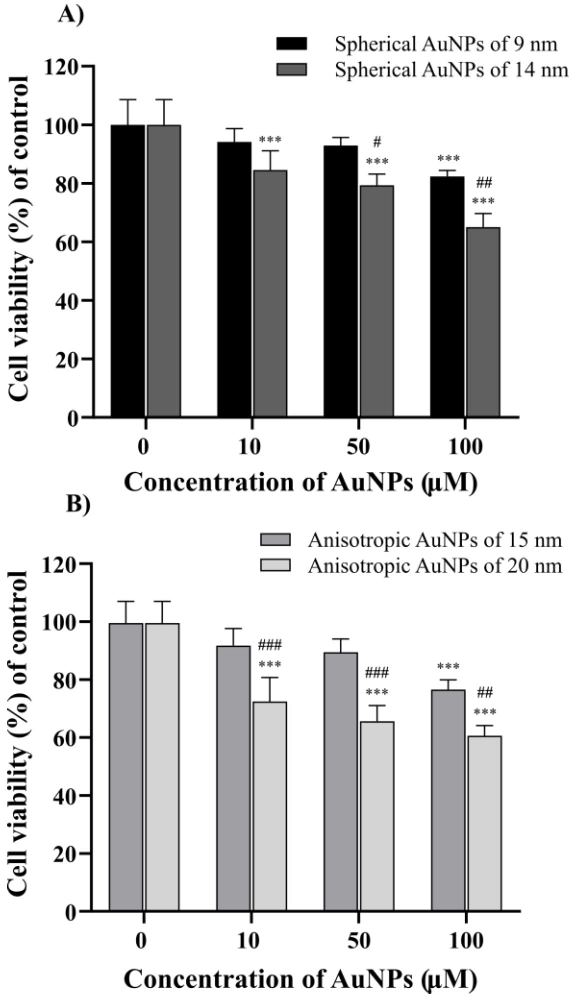

Figure 13. Cell viability assays of HeLa cells treated with A) spherical (of 9 and 14 nm) and B) anisotropic (of 15 and 20 nm), exposed to 638 nm laser at 1.56 W/cm^2 power density for 5 min. The values represent the mean ± standard deviation of three independent experiments. *denote significant difference with respect to the control: $*P < 0.05$, $**P < 0.01$, $***P < 0.001$ and $^{\#}$ denote significant difference between the sizes of AuNPs: $^{\#}P < 0.05$, $^{\#\#}P < 0.01$, $^{\#\#\#}P < 0.001$.

The photothermal effect of spherical and anisotropic AuNPs on HeLa cell viability was contrasted with cellular morphology changes evaluated through nuclear staining with Hoechst-33342 after irradiation. Changes in nuclear morphology serve to analyze cell death progression due to during apoptosis, the DNA becomes condensed, but this process does not occur during necrosis where membranes integrity is involved (Danial & Hockenbery, 2018). *Figure 14* shows the light control cells where polygonal morphology of HeLa cells and normal nucleus was observed under a fluorescence microscope. HeLa cells laser-treated with 100 μM of spherical and anisotropic AuNPs resulted in significant nuclear morphology changes in response to photothermal treatment. Phase-contrast images showed that most of the HeLa cells became circular under the irradiated AuNPs-induced stress and therefore, most of the cells lost the capacity of and progressively detached (cf. *Figure 14A-B*). The quantitative estimation of nuclear condensation and apoptotic bodies by image processing further confirmed the observation and allowed to compare the photothermal cell response with the different AuNPs tested (*Figure 14C-D*).

Again, the large spherical and anisotropic AuNPs are those that lead to bigger changes in nuclear morphology, a higher number of cells present altered morphology and the nucleus with the most condensed chromatin, even apoptotic bodies were found. 62% of HeLa cells treated with anisotropic AuNPs of 20 nm reveal significant alterations of the nucleus compared to the light control and the 14 nm spherical AuNPs. Interestingly, in *Appendix F* is observed that at 100 μM agglomerates of AuNPs are decorating HeLa cells, suggesting a significant enhancement of the photothermal effects due to the collective heating effect (Richardson, Carlson, Tandler, Hernandez, & Govorov, 2009), with a concomitant decrease in cell viability. The morphological analysis corroborates the observed trends in which cell death increases as the AuNPs concentration increases. Huang et al. (2007) also observed that aggregated gold nanospheres are responsible for the enhanced photothermal destruction of the human oral squamous cell carcinoma (HSC 3).

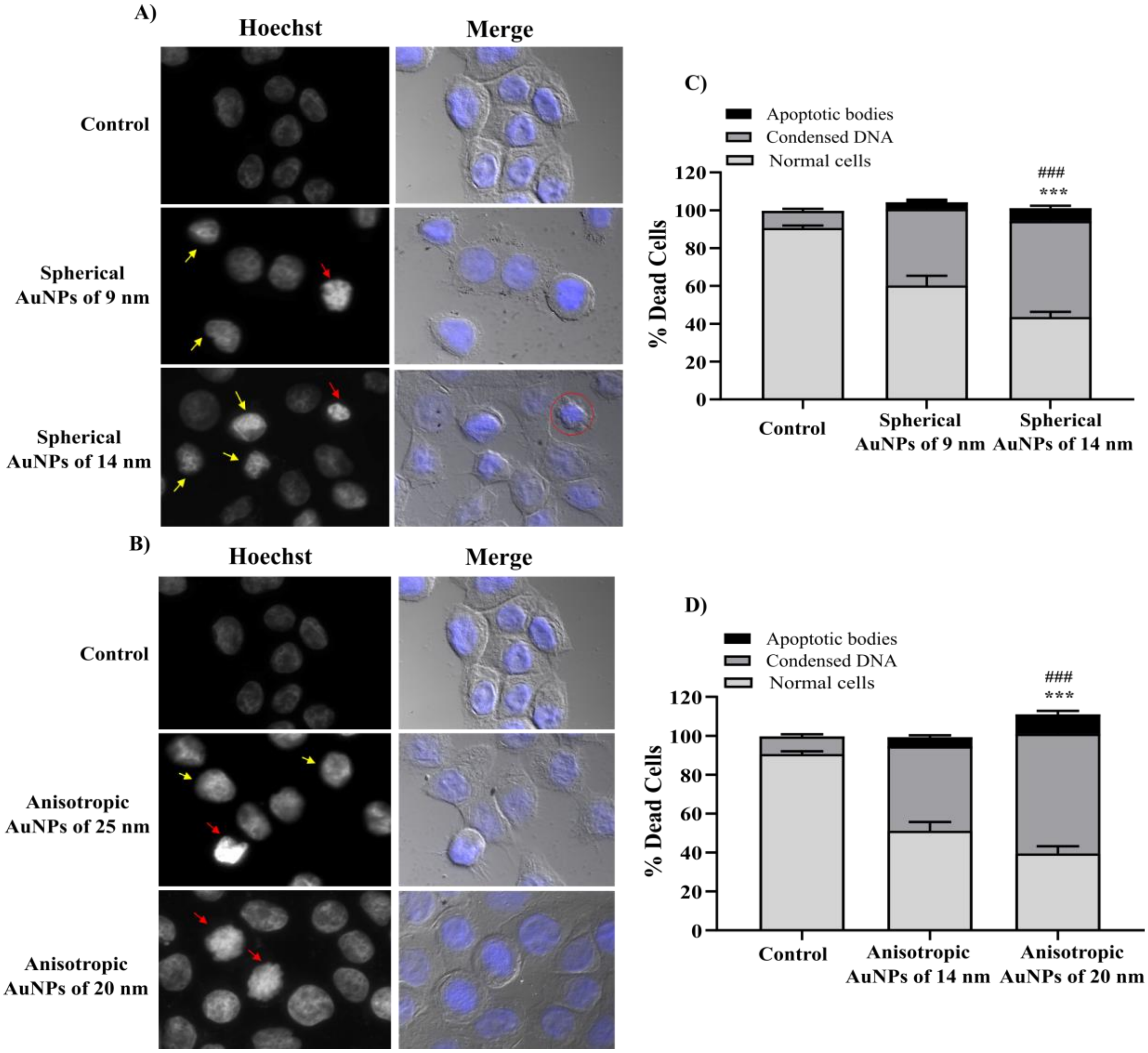

Figure 14. Nuclear staining of HeLa cells with Hoechst 33342. A) fluorescence images of HeLa treated with spherical (of 9 and 14 nm) and B) anisotropic (of 15 and 20 nm) AuNPs at 100 μM. Hoechst 33342-stained nucleus HeLa cells demonstrate typical apoptotic morphology after 5 minutes of red laser treatment with 638 nm at 1.56 W/cm^2: condensation of the nuclear material (yellow-arrow) followed by formation of apoptotic bodies (red-arrows). Original magnification: ×100. C). Quantification of damaged cells of HeLa treated with C) spherical (of 9 and 14 nm) and D) anisotropic (of 15 and 20 nm) AuNPs determined by image processing. The values represent the mean ± standard deviation of three independent experiments; *** denotes $P < 0.001$ with respect to the control; $^{###}$denotes $P < 0.001$ between sizes of AuNPs.

In order to confirm changes in cell morphology obtained from fluorescence microscopy data, transmission electron microscopy (TEM) was performed to image AuNPs in the cellular compartments and thoroughly analyze cell damage by its photothermal effect. *Figure 15* shows that in all the cases, there are intracellular uptake of AuNPs independently of its size, appearing in the form of aggregates. Dark-field images show that the AuNPs are in the cellular interior, considering the high electron density of AuNPs, located inside vesicles surrounded by a membrane (*Figure 15A*). This indicates that AuNPs tend to be encapsulated inside subcellular organelles, similar to endosomes and/or lysosomes morphology, where numerous particles are observed as aggregates. Ultrastructural examination show control HeLa cells rounded in shape without any apoptotic morphology, normal mitochondria, intact cytoplasmic, and nuclear membrane (*Figure 15B*). Whereas, treated HeLa cells showed a strong compromise to cell membranes, highlighting loss of cell membranes integrity, which is severely affected by the photothermal effect because of AuNPs are inside the cells when irradiation occurs. Therefore, the intracellular surge in temperature strongly impacts cell membrane integrity (Mendes, Pedrosa, Lima, Fernandes, & Baptista, 2017). The morphological changes observed in all treatments were reduction in cell volume and cell shrinkage. Also, membrane blebs and extensive vacuolation were observed. Because the nuclei of these cells were pyknotic, and the plasma membrane integrity was also affected, all these findings strongly suggest that the morphological changes might be events ascribable of secondary or late apoptosis and necrosis. It is in agreement with the reports of Leonidova et al. (2014), and Edinger and Thompson (2004).

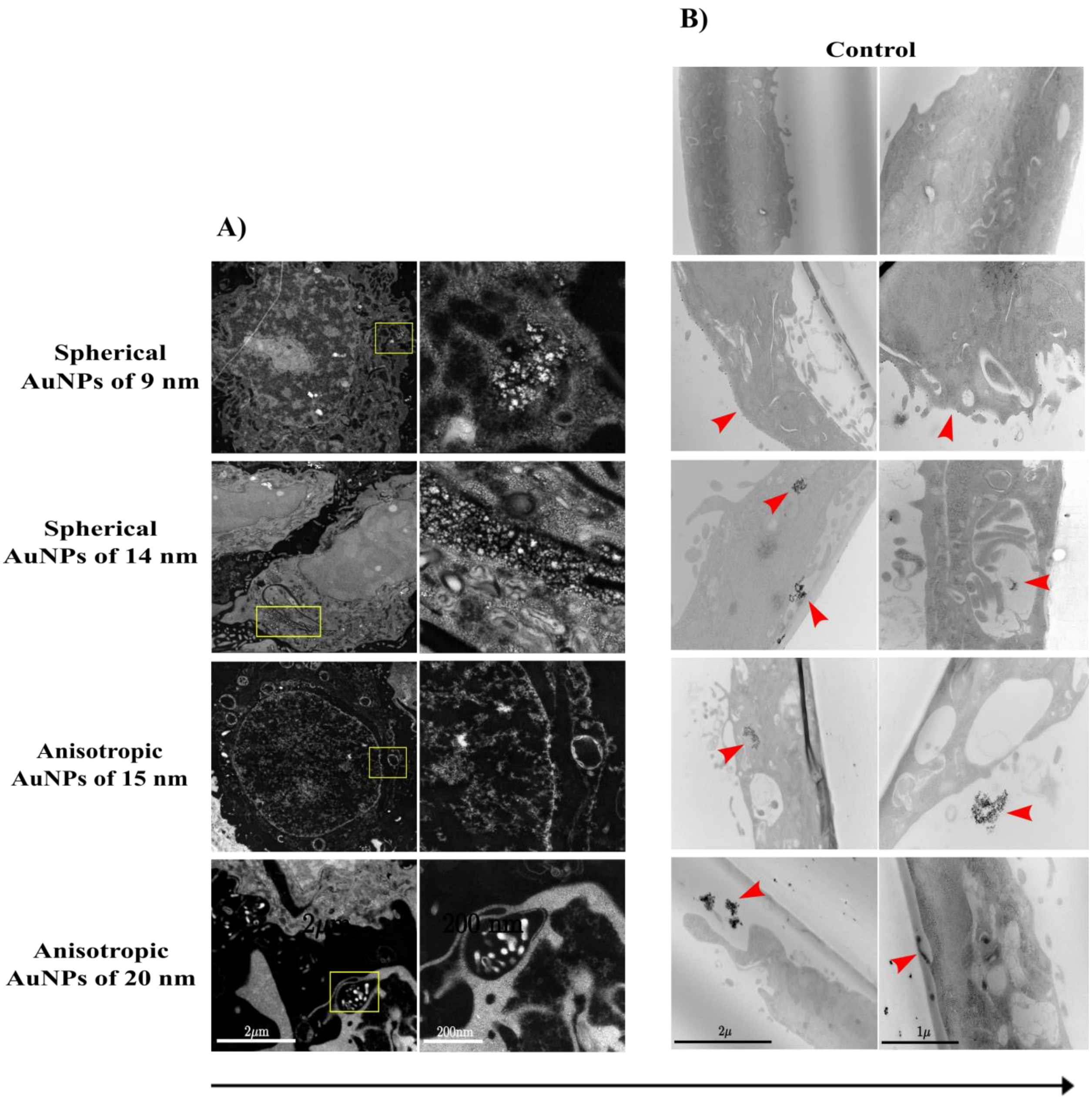

Figure 15. Transmission electron microscopy study of HeLa cell death morphology upon irradiation treatment with 630 nm at 1.56 W/cm^2 with 100 μM spherical and anisotropic AuNPs: A) High angle annular dark field (HAADF) images confirming AuNPs uptake with higher magnification images of particles plus and B) TEM images of morphological changes after laser-treated AuNPs. Electron-dense areas correspond to the AuNPs (arrowhead).

4.6 PPT compared between AuNPs and FA-AuNPs

Coherent with the insights obtained from the cellular response, we focus to the specific effects triggered of photothermal agents based on AuNPs conjugated with FA. In this study, FA-conjugated AuNPs are expected to bind to FR on the surface of HeLa cells and selectively introduced into target cells. As such, the photothermal effect on cell viability was evaluated under the same treatment conditions used for non-conjugated AuNPs by crystal violet assay. In *Figure 16,* the comparison between photothermal effect of AuNPs and AF-AuNPs on cell viability was revealed. It is important to note that a concentration-dependent response is not observed as was found with AuNPs treatment. For spherical AuNPs of 9 nm, we observed a reduction in the cell viability of 79 % just with the concentration of 50 μM. Additionally, for spherical AuNPs of 14 nm, we observed a significant reduction in cell viability 76 % with 50 μM. Likewise, at the same concentration, a reduction in cell viability of 66 % and 61 % was achieved for anisotropic AuNPs of 15 and 20 nm, respectively. Conversely, for the same unconjugated NPs a concentration of 100 μM was necessary to achieve a similar cellular response. Considering that the ligands bound to the cells in a concentration-dependent manner and reached saturation for binding (Sabharanjak & Mayor, 2004), suggests that response observed may be important for the regulated uptake of FA-AuNPs into cells. Therefore, that half the concentration with FA-AuNPs was required to achieve the highest cell death, evidences a cell receptor mediated NPs interaction in which the concentration to favor such interaction is 50 uM. Recently, Pinilla et al. in (2019) also developed and compared photothermal agents based on AgNPs and FA-conjugated AgNPs on HeLa cells. The authors suggest that FA-AgNPs reduce up to 47% the cell viability, using an 808 nm laser. This investigation conclusively revealed that FA-AgNPs are effective photothermal agents due to targeting potential of FA on HeLa cells.

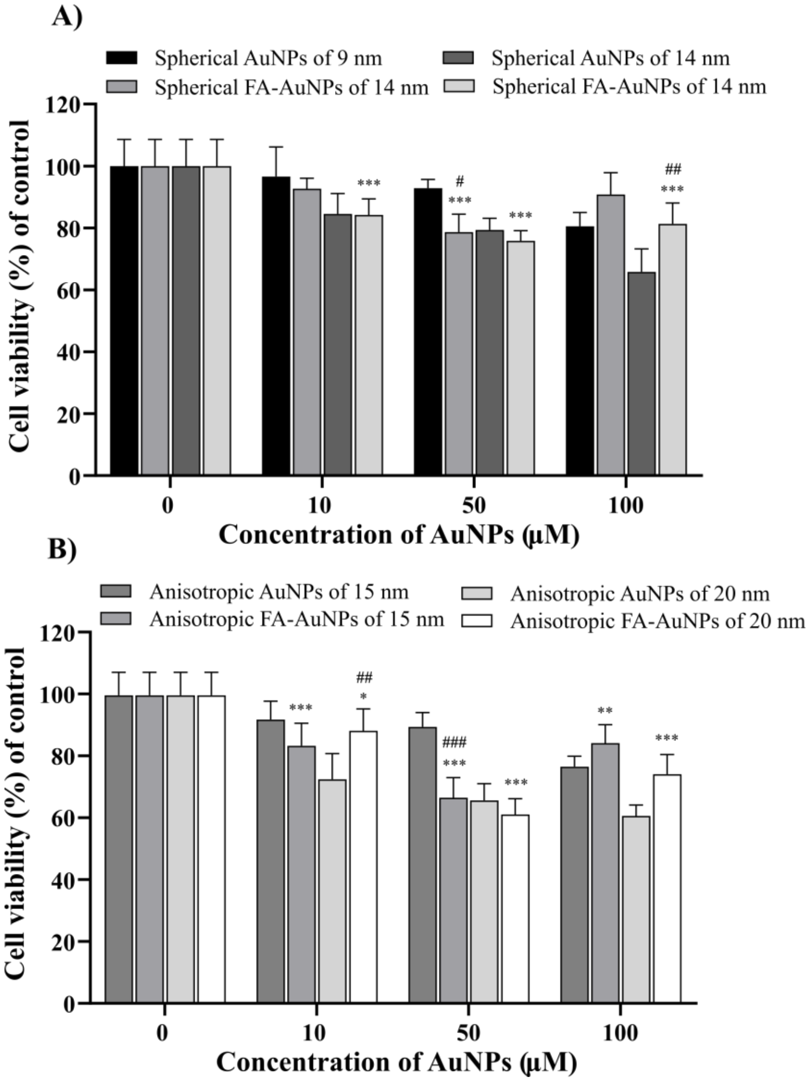

Figure 16. Cell viability assays of HeLa cells treated with various concentration of A) spherical and B) anisotropic AuNPs and FA-AuNPs, exposed to 638 nm laser at 1.56 W/cm^2 power density for 5 min. The values represent the mean ± standard deviation of three independent experiments. *denote significant difference with respect to the control: $^*P < 0.05$, $^{**}P < 0.01$, $^{***}P < 0.001$ and $^{\#}$ denote significant difference between the sizes of AuNPs: $^{\#}$denote significant difference between AuNPs and FA-AuNPs: $^{\#}P < 0.05$, $^{\#\#}P < 0.01$, $^{\#\#\#}P < 0.001$.

At a high concentration of 100 μM, viability of HeLa cells, treated with 9 and 14 nm spherical FA-AuNPs dropped to 90 % and 81 %, respectively. Likewise, a reduction of cell viability of 87

% and 74 % was found of 15 and 20 nm anisotropic FA-AuNPs treated cells, which in both cases was significantly higher than non-conjugated AuNPs. To assess the extent of the uptake of FA-AuNPs into HeLa cells, the differences in the uptake mechanism between AuNPs and FA-AuNPs were confirmed by TEM images taken after laser-treated conditions as shown in *Figure 17*. Compared to the uptake of AuNPs observed above, a greater number of FA-AuNPs can be seen distributed in the cytoplasm, these FA-AuNPs appear to escape from the endosomes and entered into the cytoplasm, suggesting that FA-AuNPs enter cells more efficiently as showed by more electron-dense areas. These results indicate that although both types of nanoparticles are taken up by HeLa cells, the FA-AuNPs induce cellular uptake and recognition distinct from the AuNPs. In certain cases, confined within cytosolic vesicles, suggesting that NPs are endocytosed probably via receptor-mediated endocytosis. From the morphological changes that occur during HeLa cell death after laser-treated FA-AuNPs, large plasma membrane blebs were observed. These blebs were presented in different types of apoptotic cells (Lane, Allan, & Woodman, 2005). Furthermore, laser-treated FA-AuNPs assay with Vero cell line were carried out to further evaluate if cellular uptake of those NPs is leading FA-receptor-expressing, since their expressions are limited in healthy Cells (zwicke2012). As it can be seen in *Appendix G,* the cells show deficient FA-AuNPs absorption and the intracellular localization was less marked than with HeLa cells. This indicates that the HeLa cellular greatly uptake of the particles is probably by the presence of FA.

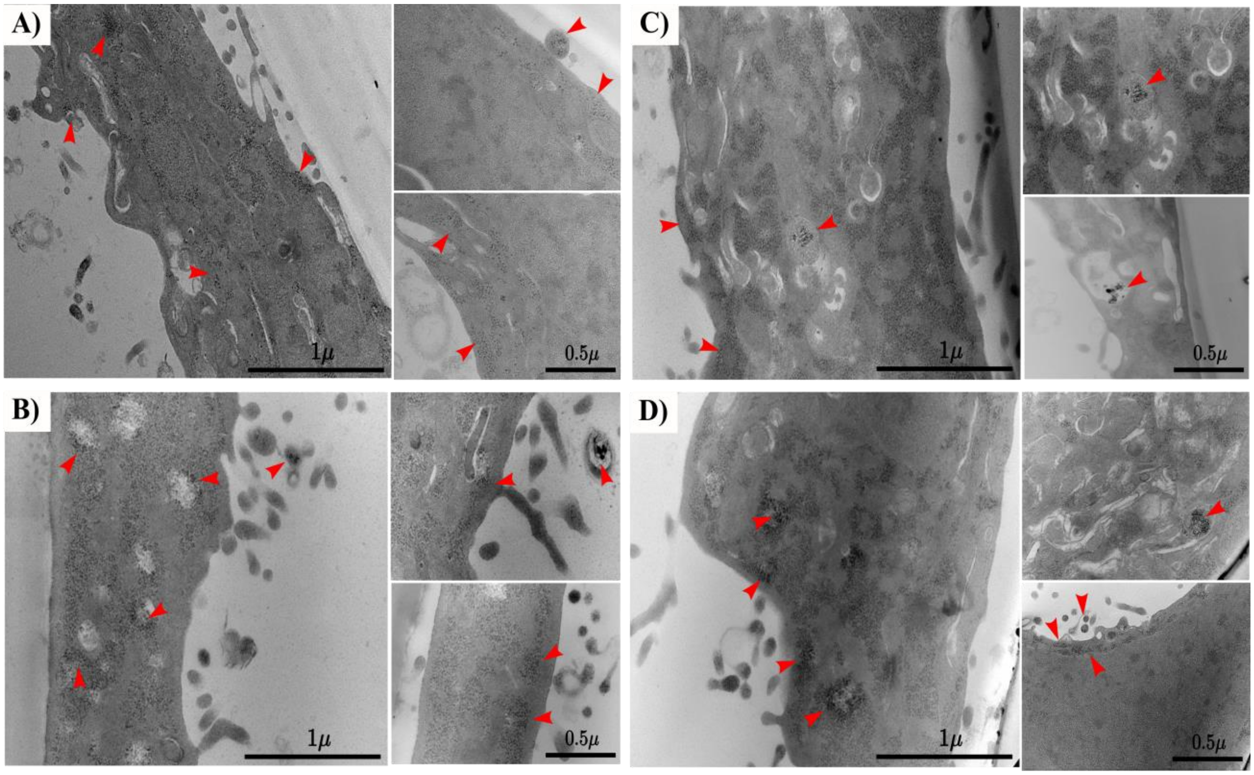

Figure 17. TEM images of FA-AuNPs distribution in HeLa cell and death morphology upon irradiation treatment with 630 nm at 1.56 W/cm^2 with 50 µM spherical and anisotropic FA-AuNPs: A) spherical FA-AuNPs of 9 nm, B) spherical FA-AuNPs of 14 nm, C) anisotropic FA-AuNPs of 15 nm and D) anisotropic FA-AuNPs of 20 nm. Electron-dense areas correspond to the FA-AuNPs (arrowhead).

To gain insight in the role of FA on cell death mediated by photothermal effect, a flow-cytometric assay was carried out to distinguish the mode of cell death upon exposure to activated AuNPs and FA-AuNPs after irradiation. Annexin V/7-amino-actinomycin (7-AAD) dyes were used to stain and exclude between early apoptosis, late apoptosis and necrosis. Annexin V successfully labels cells during early apoptosis which binds to phosphatidylserine (PS) on the outer side of the plasma membrane. Late apoptotic cells and necrotic cells lose their cell membrane integrity and are permeable to 7-AAD that selectively binds to GC regions of the DNA (Zembruski, Stache, Haefeli, & Weiss, 2012). Therefore, stained cells were analyzed through the flow cytometer and the existence of four population were distinguished from the following criteria: viable cells are annexin V and 7-AAD negative, early apoptotic cells are annexin V positive and 7-AAD negative, late stage apoptotic and necrotic are annexin V and 7-AAD positive, and death cells (mostly nuclear debris) are annexin V negative and 7-AAD positive (Card, n.d). The percentage of populations were generated from dot plots and processed as bar graph (cf. *Figure 18*). As expected, treatment of HeLa cells with all types of AuNPs and AF-AuNPs result in percentage of viable cells comparable to our cell viability assay results using same NPs concentration. It is important to recognize that no differences were found in the mechanisms of cell death related to the size and shape of AuNP tested. This makes sense because the phenomenon that is sought to mediate cell death is the photothermal effect of AuNP, so changes in the amount of cell death are expected due to its photothermal efficiency and no differences in the pathway of cell death. Interestedly, the response of HeLa cells to FA-AuNPs was thoroughly different from AuNPs. Treatment with spherical FA-AuNPs of 9 and 14 nm caused the cells entering late apoptosis increased by 5 % and 8 %, respectively. With the same non-conjugated AuNPs, the cells were found in late apoptosis population to eventually undergo majority death cell. In this population, the plasma membrane loses its integrity and then, the cell is fragmented into nuclear debris forms in the necrosis process (Kepp, Galluzzi, Lipinski, Yuan, & Kroemer, 2011). The cells become permeable for 7-AAD either immediately or shortly after through early apoptosis, therefore these results suggest that cells are in fact traversing through late apoptosis/necrosis as a result of cells died via necrosis but not through the apoptotic pathway. It is widely known that cell death triggered by PPT mainly induces necrosis, which is characterized by loss of plasma membrane integrity and the release of intracellular contents into surrounding tissues leading to a detrimental inflammatory and immunogenic responses (Martin, Henry, & Cullen, 2012) that clearly reduces the treatment efficiency.

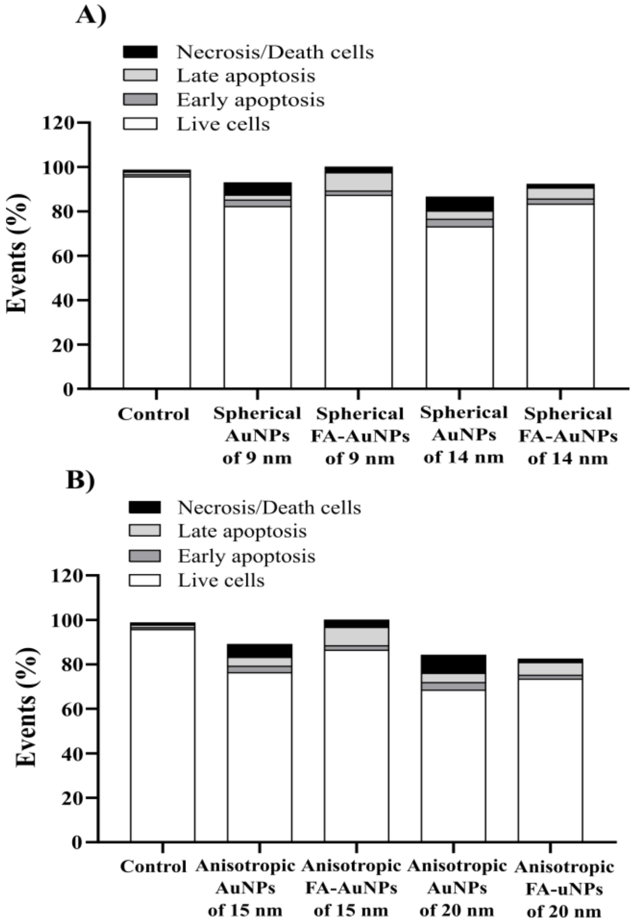

Figure 18. Annexin V and 7-AAD staining of HeLa cells treated with different AuNPs and FA-AuNPs solution at 100 μM for 4 h and exposed to 638 nm laser at 1.56 W/cm^2 power density for 5 min. Bar graph showing the rates of apoptosis and necrosis of HeLa cells in the individual groups. Cells stained with 7-AAD alone are necrotic, whereas cells stained with Annexin V alone represent early apoptosis. Cells at the final stage of apoptosis take up both staining.

Conversely, an indicator of either increased transition of early apoptotic cells to late apoptosis/necrosis were not observed with FA-conjugated AuNPs treatment, the cells appears in the late stages of apoptosis or dead. In the same way, treatment with anisotropic FA-AuNPs of 15 and 20 nm, the percentage of late apoptosis was higher than the anisotropic non-conjugated AuNPs, in which the largest population was found in final state of cell death. Although in the case of FA-AuNPs treatments, Annexin V/7-AAD staining does not distinguish between cells that have undergone apoptotic death versus those that have died as a result of a necrotic pathway since in either case dead cells will be stained by both labeled annexin V and 7-AAD (Zimmermann & Meyer, 2011), these results show that cells are in fact traversing through early apoptosis before reaching late apoptosis/necrosis which further confirm that laser-treated FA-AuNPs induced cell death by apoptotic mechanism. Therefore, it is noticeable that the mechanism of uptake of AF-AuNPs and, therefore, its subsequent processing by HeLa cells as well as its photothermal effect could be different from AuNPs.

Previous reports established that reactive oxygen species (ROS) can be produced in response to heat stress during PPT treatment and mediated cell death in various cancer cells by different NPs (Chompoosor et al., 2010; Kuo, Chang, Cho, Chiu, Lien, Yeh, Chen, et al., 2012; Kuo, Chang, Cho, Chiu, Lien, Yeh, & Chen, 2012). Thereby, we were interested to probe if ROS would be generated in HeLa cells treated with AuNPs and FA-AuNPs before and after laser exposure. In this sense, the production of ROS during PPT treatment with spherical AuNPs of 14 nm and spherical FA-AuNPs of 14 nm was investigated using a fluorescent 2,7-dichlorofluorescein (DCF) assay to measure the reactive oxygen levels in cell culture media before and after treatment. Again, HeLa cells were treated with AuNPs dispersed in the cell culture media. After 4 h of incubation, the cells were exposed to the 650 nm laser to induce photothermal heating. The treatment was performed using 14 nm spherical AuNPs because induced slightly greater cell death than the smallest tested. Finally, the DCF assay was used to measure the amount of ROS present in the cell media before and after laser exposure. As *Figure 19* shows, the incubation of HeLa cells with AuNPs and AF-AuNPs alter the amount of endogenous ROS present in the control in a dependent manner on the AuNPs conjugation before laser exposure. Particularly, incubation with AuNPs led to a significant incremented in ROS levels compared to untreated control, the amount of ROS present in AF-AuNPs containing cell media was negligible. However, cell viability tests did not show intrinsic cytotoxicity for any of the AuNPs, therefore, exposure to these AuNPs themselves are not necessarily detrimental to cellular function as endogenous ROS exert an important role in "redox" signaling pathways that contribute to normal cell function (Rhee, 2006). After laser exposure, the amount of ROS in culture media containing AuNPs displayed a highly significant increase in fluorescence, confirming the formation of ROS during PPT treatment. It is important to note that the incremented of the ROS levels is again higher than observed with FA-AuNP. The control cells without AuNPs or FA-AuNPs did not show any significant changes in fluorescence after laser exposure, indicating that the ROS formed during PPT treatment were produced by these AuNPs and, in addition, that control cell did not display a significant thermal response as previously confirmed. Accordingly, non-conjugated AuNPs displayed the strongest thermal response to PPT, besides the significant amounts of ROS produced during the treatment, resulting in cell death through oxidative damage, in addition to the toxicity induced by hyperthermia. Comparable heat stress-induced ROS production, and accordingly cell death, would be expected with laser-treated FA-AuNPs. However, FA-AuNPs displayed the weakest thermal response to PPT treatment, and they also reduced any ROS produced during the treatment before oxidative damage could occur. The lack of cell death from the FA-AuNPs-treated samples further confirms the effective protective effect of ROS by the FA shell. The presence of FA reduce any ROS produced during treatment and even before laser exposure (cf. *Figure 19*), making ineffectively the sensitize cancer cell to make them highly vulnerable to subsequent hyperthermia, resulting in observed marginal efficiency.

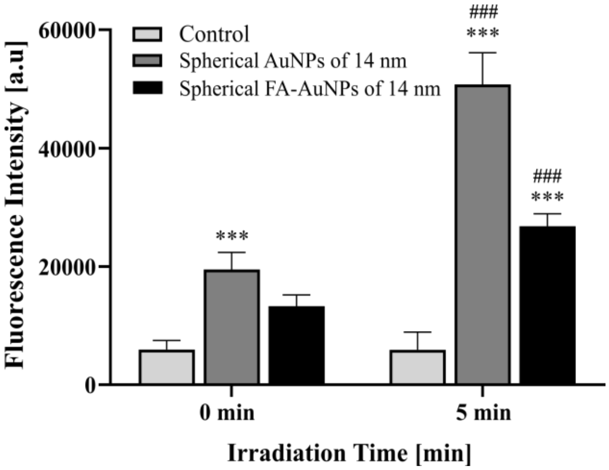

Figure 19. Quantitative measurements of ROS generation in cell media before 0 min and after 5 min of photothermal heating. Medium from 14 nm spherical AuNPs and FA-AuNPs treated cells show more ROS due to increment of endogenous oxygen. After heating, medium from AuNPs-treated cells show significantly higher ROS levels due to heat stress. FA-AuNPs show significant diminished in ROS levels, indicating that the reactive species are reduced before cell damage occurs. The values represent the mean ± standard deviation of three independent experiments; ***denotes $P < 0.001$ with respect to the control; $^{###}$denotes $P < 0.001$ between laser-treated AuNPs and non-irradiated treated-AuNPs.

These results are in agreement with the derivatives in flow cytometry assay, as unconjugated AuNPs after laser exhibit high production of ROS which can increase the regulation of caspase protein to initiate cell apoptosis as observed (Fink, immunity, & 2005, n.d.). Although, the apoptosis and necrosis are not necessarily mutually exclusive, as demonstrated by high oxidative stress, where mixed death phenotypes have been observed (Ryter et al., 2007). Our findings confirm that laser-treated FA-AuNPs induced apoptosis rather than necrosis reduced concerns regarding of side effect caused by inflammatory cellular response in necrosis pathway (Melamed, Edelstein, & Day, 2015). In addition to the fact that FA seems to play protective effect on oxidative stress. Taken together, these results indicate that AuNPs as well as FA-AuNPs can be employed not only as a source of heat but also as photosensitizers mediating generation of ROS under irradiation. The production of ROS is likely to produce a synergistic effect in combination with hyperthermia that results in effective cell death, further supporting the conclusion that ROS play a significant role during PPT treatment. In contrast, FA-conjugated AuNPs triggered synergistic effects between induces cell death by apoptosis while reducing the risk of undesirable side effects due to heat stress induced ROS formation during treatment.

5 Conclusions

A useful effect was observed in nanoparticles synthesized in cationic reverse micelles of CTAB when the environment at the interface is modified by changing the organic solvent. It was found that the particle size, morphology and plasmon absorption band are affected as a result of kinetics and growth mechanism changes. When *n*-hexane was used as a continuous phase, the particle size decreased at higher intermicellar exchange rate favoring particles isotropic growth which lead to the formation of monodisperse spherical AuNPs. Otherwise, when toluene was employed as the continuous phase, it was observed that its molecular bulkiness makes the intermicellar interaction less efficient, together with the binding of (Br^-) ions available at its interface on gold surfaces, they are the key factor that increments particle size and induces anisotropic growth in AuNPs obtained. Therefore, it means that the effects of reverse micellar interfaces comprise a simple way to control optical properties of AuNPs.

Our results demonstrated that the dynamic character of these reverse micellar media, used as a nanoreactor, is an important feature to take in account for increasing our understanding about nanoparticles synthesis in nanoconfined systems. Moreover, they provide insight into easy optical tunability and simple synthesis of AuNPs, which can combine with well-known superior visible and near-infrared light absorption as well as scattering. Furthermore, this offers a useful cell uptake and potential non-cytotoxicity, which makes AuNPs the most promising agents for biomedical applications, such as photothermal therapy.

Finally, we found that the photothermal properties of AuNPs can be modulated trough variation of the size, shape, and surface conjugation to induce efficient cell death in PPT. Here, we showed that large spherical and anisotropic AuNPs exhibited significantly enhanced photothermal effects when irradiated with a red laser in comparison to the smallest AuNPs tested. At 100 μM, the viability of HeLa cells dropped significantly to 65 % and 60 %, after laser-treated with 14 nm spherical and 20 nm anisotropic AuNPs, respectively. The reduction of HeLa cell viability is ascribed to a synergetic effect of AuNPs between the production of ROS which is likely to give rise in combination with stress by photothermal heating. Importantly, the AuNPs did not induce cell death by themselves, confirming their biocompatibility, and induce cell death upon laser exposure, verifying their usefulness as photothermal agents. These AuNPs were used to demonstrate the targeted photothermal treatment after the incorporation of FA-conjugated AuNPs. The observed viabilities were <70% in the cases for FA-AuNPs at 50 μM. It is advantageous because lower concentrations of FA-AuNPs are required to achieve the same cellular effect achieved with unconjugated laser-treatment AuNPs. In fact, the conjugated agent not only exhibited an effect on the uptake and toxicity of NPs, but also diminished ROS levels after laser-treated FA-AuNPs in culture medium, which conferred an additional advantage due to promote protective stress pathways preventing unwanted death as a result of heat-stress-induced ROS formation and therefore their death signalings are different from AuNPs. More broadly, our findings exhibit a promising approach to achieving cancer cells die, which are ascribed to the sensitization effect arising from plasmon-mediated ROS, which clearly plays a crucial role in enhancing the PPT efficacy.

6 Future works

- To explore the conjugation with folic acid by variations of nanoparticle-folic acid interaction through pH changes or the addition of ligands to facilitate a stronger non-covalent conjugation, which could contribute to the general understanding of the FA-AuNPs cellular uptake.
- To evaluate the obtained in vitro photothermal effect on healthy cells, in order to confirm if that functionalization with folic acid is a key factor in the selectivity of photothermal therapy.

7 Results communications

The results of this research were presented in national and international scientific congress.

- Guerrero-Florez, V. Martínez-Ortega, F. Méndez-Sanchez S. “Hipertermia Óptica Mediada por Nanopartículas de Oro sobre Células de Adenocarcinoma de Cérvir (HeLe)”. In IX Escuela Internacional de NanoAndes, Oct. 2019, Santiago de Chile.
- Guerrero-Florez, V. Martínez-Ortega, F. Blach, D. Cationic Reverse Micelles as a Nano-reactors of Gold Nanoparticles. In VIII Escuela Internacional de NanoAndes, Nov. 2018, Mexico.
- Guerrero-Florez, V. Martínez-Ortega, F. Blach, D. Size dependence of photothermal heat generation on gold nanoparticles. In 5th Latin-American Congress of Photocatalysis, Photoelectrochemistry and Photobiology, Nov. 2017, Mexico.

- Guerrero-Florez, V. Martínez-Ortega, F. Blach, D. Méndez-Sanchez S. Cell Viability Assay of HeLa with Gold Nanoparticles. In “Primer Encuentro Internacional en Ciencias de la Salud: el saber y la tecnología al servicio de la vida”, Jun. 2017, Colombia.
- Guerrero-Florez, V. Martínez-Ortega, F. Blach, D. Effect of cationic CTAB interface composition on the formation and final properties of gold nanoparticles. In Workshop on Nanotechnology in Characterization, Metrology, Manufacturing and Safety, Feb. 2017, Colombia-U.S.

Bibliographic references

Acceptors, B., Levitt, M., & Perutz, M. F. (1988). Rings Act as Hydrogen. *Journal of Molecular Biology*, *201*(4), 751–754. https://doi.org/http://dx.doi.org/10.1016/0022-2836(88)90471-8

Acres, R. G., Feyer, V., Tsud, N., Carlino, E., & Prince, K. C. (2014). Mechanisms of aggregation of cysteine functionalized gold nanoparticles. *Journal of Physical Chemistry C*, *118*(19), 10481–10487. https://doi.org/10.1021/jp502401w

Aioub, M., Panikkanvalappil, S. R., & El-Sayed, M. A. (2017). Platinum-Coated Gold Nanorods: Efficient Reactive Oxygen Scavengers That Prevent Oxidative Damage toward Healthy, Untreated Cells during Plasmonic Photothermal Therapy. *ACS Nano*, *11*(1), 579–586. https://doi.org/10.1021/acsnano.6b06651

Albanese, A., Tang, P. S., & Chan, W. C. W. (2012). The Effect of Nanoparticle Size, Shape, and Surface Chemistry on Biological Systems. *Annual Review of Biomedical Engineering*, *14*(1), 1–16. https://doi.org/10.1146/annurev-bioeng-071811-150124

Angelomé, P. C., Mezerji, H. H., Goris, B., Pastoriza-Santos, I., Pérez-Juste, J., Bals, S., & Liz-Marzán, L. M. (2012). Seedless synthesis of single crystalline Au nanoparticles with unusual shapes and tunable LSPR in the near-IR. *Chemistry of Materials*, *24*(7), 1393–1399. https://doi.org/10.1021/cm3004479

ANKER, J. N., HALL, W. P., LYANDRES, O., SHAH, N. C., ZHAO, J., & VAN DUYNE, R. P. (2009). Biosensing with plasmonic nanosensors. In *Nanoscience and Technology* (pp. 308–319). Co-Published with Macmillan Publishers Ltd, UK. https://doi.org/10.1142/9789814287005_0032

Antony, A. C. (1992). The Biological Chemistry of Folate Receptors HE ESSENTIAL role of intracellular folates in ef, *79*(11), 2807–2820. Retrieved from https://pdfs.semanticscholar.org/04a6/b39e39545619cdd92a3142dc307285fd61a5.pdf

Bagwe, R. P., & Khilar, K. C. (1997). Effects of the Intermicellar Exchange Rate and Cations on the Size of Silver Chloride Nanoparticles Formed in Reverse Micelles of AOT. *Langmuir*, *13*(24), 6432–6438. https://doi.org/10.1021/la9700681

Bancroft, W. D., & Gurchot, C. (2005). The Scattering of Light. *The Journal of Physical Chemistry, 36*(10), 2575–2587. https://doi.org/10.1021/j150340a005

Batchelor, R. (2008). Photodynamic therapy for the treatment of morphoea. *Clinical and Experimental Dermatology*, *33*(5), 661–663. https://doi.org/10.1111/j.1365-2230.2008.02873.x

Blach, D, Correa, N., Silber, J., science, R. F. and interface, & 2011, undefined. (n.d.). Interfacial water with special electron donor properties: Effect of water–surfactant interaction in confined reversed micellar environments and its influence on the. *Elsevier*. Retrieved from https://www.sciencedirect.com/science/article/pii/S0021979710013457

Blach, Diana, & Martínez, F. O. (2017). Gold nanoparticles optical properties induced by water and an ionic liquid (bmimBF 4) inside cationic reverse micelles. *New Journal of Chemistry*, *41*(21), 13104–13113. https://doi.org/10.1039/c7nj01106g

Card, Q. R. (n.d.-a). Muse^{TM} Annexin V & Dead Cell Kit User's Guide, *100105*(4700), 100105–100106.

Card, Q. R. (n.d.-b). Muse^{TM} Annexin V & Dead Cell Kit User's Guide.

Cason, J. P., Miller, M. E., Thompson, J. B., & Roberts, C. B. (2001). Solvent Effects on Copper Nanoparticle Growth Behavior in AOT Reverse Micelle Systems. *The Journal of Physical Chemistry B*, *105*(12), 2297–2302. https://doi.org/10.1021/jp002127g

Castillo, J. J., Rindzevicius, T., Rozo, C. E., & Boisen, A. (2015). Adsorption and vibrational study of folic acid on gold nanopillar structures using surface-enhanced raman scattering spectroscopy. *Nanomaterials and Nanotechnology*, *5*(1). https://doi.org/10.5772/61606

Cazabat, A. M., & Langevin, D. (1981). Diffusion of interacting particles: Light scattering study of microemulsions. *The Journal of Chemical Physics*, *74*(6), 3148–3158. https://doi.org/10.1063/1.441525

Celli, J. P., Spring, B. Q., Rizvi, I., Evans, C. L., Samkoe, K. S., Verma, S., … Hasan, T. (2010). Imaging and Photodynamic Therapy: Mechanisms, Monitoring, and Optimization. *Chemical Reviews, 110*(5), 2795–2838. https://doi.org/10.1021/cr900300p

Chandler, D. (2005). Interfaces and the driving force of hydrophobic assembly. *Nature*, *437*(7059), 640–647. https://doi.org/10.1038/nature04162

Chen, D.-H., & Wu, S.-H. (2000). Synthesis of Nickel Nanoparticles in Water-in-Oil Microemulsions. *Chemistry of Materials*, *12*(5), 1354–1360. https://doi.org/10.1021/cm991167y

Chen, F., Xu, G. Q., & Hor, T. S. A. (2003). Preparation and assembly of colloidal gold nanoparticles in CTAB-stabilized reverse microemulsion. *Materials Letters*, *57*(21), 3282–3286. https://doi.org/10.1016/S0167-577X(03)00048-X

Chiang, C. L., Hsu, M. B., & Lai, L. B. (2004). Control of nucleation and growth of gold nanoparticles in AOT/Span80/isooctane mixed reverse micelles. *Journal of Solid State Chemistry, 177*(11), 3891–3895. https://doi.org/10.1016/j.jssc.2004.07.003

Chithrani, B. D., Ghazani, A. A., & Chan, W. C. W. (2006). Determining the size and shape dependence of gold nanoparticle uptake into mammalian cells. *Nano Letters, 6*(4), 662–668. https://doi.org/10.1021/nl052396o

Chompoosor, A., Saha, K., Ghosh, P. S., MacArthy, D. J., Miranda, O. R., Zhu, Z. J., … Rotello, V. M. (2010). The role of surface functionality on acute cytotoxicity, ROS generation and DNA damage by cationic gold nanoparticles. *Small*, *6*(20), 2246–2249. https://doi.org/10.1002/smll.201000463

Connor, E. E., Mwamuka, J., Gole, A., Murphy, C. J., & Wyatt, M. D. (2005). Gold Nanoparticles Are Taken Up by Human Cells but Do Not Cause Acute Cytotoxicity. *Small*, *1*(3), 325–327. https://doi.org/10.1002/smll.200400093

Crans, D. C., Rithner, C. D., Baruah, B., Gourley, B. L., & Levinger, N. E. (2006). Molecular probe location in reverse micelles determined by NMR dipolar interactions. *Journal of the*

American Chemical Society, *128*(13), 4437–4445. https://doi.org/10.1021/ja0583721

Crans, D. C., Schoeberl, S., Gaidamauskas, E., Baruah, B., & Roess, D. A. (2011). Antidiabetic vanadium compound and membrane interfaces: Interface-facilitated metal complex hydrolysis. *Journal of Biological Inorganic Chemistry*, *16*(6), 961–972. https://doi.org/10.1007/s00775-011-0796-5

Curri, M. L., Agostiano, A., Manna, L., Monica, M. Della, Catalano, M., Chiavarone, L., … Lugarà, M. (2000). Synthesis and Characterization of CdS Nanoclusters in a Quaternary Microemulsion: the Role of the Cosurfactant. *The Journal of Physical Chemistry B*, *104*(35), 8391–8397. https://doi.org/10.1021/jp0007639

Danial, N. N., & Hockenbery, D. M. (2018). *Chapter 18 - Cell Death*. *Hematology* (Seventh Ed). Elsevier Inc. https://doi.org/10.1016/B978-0-323-35762-3.00018-4

de Aberasturi, D. J., Serrano-Montes, A. B., & Liz-Marzán, L. M. (2015). Modern Applications of Plasmonic Nanoparticles: From Energy to Health. *Advanced Optical Materials*, *3*(5), 602–617. https://doi.org/10.1002/adom.201500053

De, T., science, A. M.-A. in colloid and interface, & 1995, undefined. (n.d.). Solution behaviour of Aerosol OT in non-polar solvents. *Elsevier*. Retrieved from https://www.sciencedirect.com/science/article/pii/000186869580005N

Decuzzi, P., & Ferrari, M. (2008). The receptor-mediated endocytosis of nonspherical particles. *Biophysical Journal*, *94*(10), 3790–3797. https://doi.org/10.1529/biophysj.107.120238

Di Felice, R., & Selloni, A. (2004). Adsorption modes of cysteine on Au(111): Thiolate, amino-thiolate, disulfide. *Journal of Chemical Physics*, *120*(10), 4906–4914. https://doi.org/10.1063/1.1645789

Dokter, A. M., Woutersen, S., & Bakker, H. J. (2007). Ultrafast dynamics of water in cationic micelles. *Journal of Chemical Physics*, *126*(12), 1–11. https://doi.org/10.1063/1.2721527

Drofenik, M. (2005). Synthesis of materials within reverse micelles ´Drofenik, M. (2005).

Synthesis of materials within reverse micelles ´ ∗, 12(2), 239–277. ∗, *12*(2), 239–277.

Eastoe, J., Hollamby, M. J., & Hudson, L. (2006a). Recent advances in nanoparticle synthesis with reversed micelles. *Advances in Colloid and Interface Science, 128–130*(2006), 5–15. https://doi.org/10.1016/j.cis.2006.11.009

Eastoe, J., Hollamby, M. J., & Hudson, L. (2006b). Recent advances in nanoparticle synthesis with reversed micelles. *Advances in Colloid and Interface Science, 128–130*(2006), 5–15. https://doi.org/10.1016/j.cis.2006.11.009

Edinger, A. L., & Thompson, C. B. (2004). Death by design: Apoptosis, necrosis and autophagy. *Current Opinion in Cell Biology*, *16*(6), 663–669. https://doi.org/10.1016/j.ceb.2004.09.011

Fang, X., & Yang, C. (1999). An Experimental Study on the Relationship between the Physical Properties of CTAB/Hexanol/Water Reverse Micelles and ZrO2-Y2O3 Nanoparticles Prepared. *Journal of Colloid and Interface Science*, *212*, 242–251. https://doi.org/10.1006/jcis.1998.6038

Faraday, M. (1857). X. The Bakerian Lecture. —Experimental relations of gold (and other metals) to light. *Philosophical Transactions of the Royal Society of London*, *147*, 145–181. https://doi.org/10.1098/rstl.1857.0011

Fazary, A. E. (2013). Ionic strength dependence of four stepwise protonation constants for folic acid in different aqueous solutions of dioxane. *Journal of Chemical and Engineering Data*, *58*(8), 2219–2223. https://doi.org/10.1021/je4002569

Federico M. Agazzi, R. Dario Falcone, Juana J. Silber, N. M. C. (2011). Solvent Blends can Control Cationic Reversed Micellar Interdroplet Interactions. The Effect of. *J. Phys. Chem.*, *115*, 12076–12084.

Feoktistova, M., Geserick, P., & Leverkus, M. (2016). Crystal violet assay for determining viability of cultured cells. *Cold Spring Harbor Protocols*, *2016*(4), 343–346. https://doi.org/10.1101/pdb.prot087379

Filankembo, A., Giorgio, S., Lisiecki, I., & Pileni, M. P. (2003). Is the Anion the Major Parameter in the Shape Control of Nanocrystals? † . *The Journal of Physical Chemistry B*, *107*(30), 7492–7500. https://doi.org/10.1021/jp022282q

Fink, S., immunity, B. C.-I. and, & 2005, undefined. (n.d.). Apoptosis, pyroptosis, and necrosis: mechanistic description of dead and dying eukaryotic cells. *Am Soc Microbiol*. Retrieved from https://iai.asm.org/content/73/4/1907.short

Fletcher, P. D. I., Howe, A. M., & Robinson, B. H. (1987). The kinetics of solubilisate exchange between water droplets of a water-in-oil microemulsion. *Journal of the Chemical Society, Faraday Transactions 1: Physical Chemistry in Condensed Phases*, *83*(4), 985–1006. https://doi.org/10.1039/F19878300985

Gaidamauskas, E., Cleaver, D. P., Chatterjee, P. B., & Crans, D. C. (2010). Effect of micellar and reverse micellar interface on solute location: 2,6-pyridinedicarboxylate in ctab micelles and ctab and aot reverse micelles. *Langmuir*, *26*(16), 13153–13161. https://doi.org/10.1021/la101579f

Ganguli, A. K., Ganguly, A., & Vaidya, S. (2010). Microemulsion-based synthesis of nanocrystalline materials. *Chemical Society Reviews*, *39*(2), 474–485. https://doi.org/10.1039/b814613f

Gans, R. (1912). Über die Form ultramikroskopischer Goldteilchen. *Annalen Der Physik, 342*(5), 881–900. https://doi.org/10.1002/andp.19123420503

García-Río, L., Godoy, A., & Rodríguez-Dafonte, P. (2006). Influence of the oil on the properties of microemulsions as reaction media. *European Journal of Organic Chemistry*, (15), 3364–3371. https://doi.org/10.1002/ejoc.200600086

Giustini, M., Palazzo, G., Colafemmina, G., Della Monica, M., Giomini, M., & Ceglie, A. (1996). Microstructure and Dynamics of the Water-in-Oil CTAB/ *n* -Pentanol/ *n* -Hexane/Water Microemulsion: A Spectroscopic and Conductivity Study. *The Journal of Physical Chemistry*, *100*(8), 3190–3198. https://doi.org/10.1021/jp952263z

Gómez-Graña, S., Hubert, F., Testard, F., Guerrero-Martínez, A., Grillo, I., Liz-Marzán, L. M., & Spalla, O. (2012). Surfactant (Bi) layers on gold nanorods. *Langmuir*, *28*(2), 1453–1459. https://doi.org/10.1021/la203451p

González-Blanco, C., Rodríguez, L. J., & Velázquez, M. M. (2002). Effect of the Addition of Water-Soluble Polymers on the Structure of Aerosol OT Water-in-Oil Microemulsions: A Fourier Transform Infrared Spectroscopy Study. *Langmuir*, *13*(7), 1938–1945. https://doi.org/10.1021/la960451q

Gu, F. X., Karnik, R., Wang, A. Z., Alexis, F., Levy-nissenbaum, E., Hong, S., … Farokhzad, O. C. (2007). Targeted nanoparticles Over the past decade , there has been an increasing interest in using fabrication of targeted NPs using microfluidic devices . *Nano Today*, *2*(3), 14–21.

Gutierrez, J. A., Falcone, R. D., Lopez-Quintela, M. A., Buceta, D., Silber, J. J., & Correa, N. M. (2014). On the investigation of the droplet-droplet interactions of sodium 1,4-bis(2-ethylhexyl) sulfosuccinate reverse micelles upon changing the external solvent composition and their impact on gold nanoparticle synthesis. *European Journal of Inorganic Chemistry*, (12), 2095–2102. https://doi.org/10.1002/ejic.201301612

Ha, T. H., Koo, H. J., & Chung, B. H. (2007). Shape-controlled syntheses of gold nanoprisms and nanorods influenced by specific adsorption of halide ions. *Journal of Physical Chemistry C*, *111*(3), 1123–1130. https://doi.org/10.1021/jp066454l

Hait, S. K., Sanyal, A., & Moulik, S. P. (2002). Physiochemical studies on microemulsions. 8. The effects of aromatic methoxy hydrotropes on droplet clustering and understanding of the dynamics of conductance percolation in water/oil microemulsion systems. *Journal of Physical Chemistry B*, *106*(48), 12642–12650. https://doi.org/10.1021/jp026702n

Hodak, José H., Martini, I., & Hartland, G. V. (2002). Spectroscopy and Dynamics of Nanometer-Sized Noble Metal Particles. *The Journal of Physical Chemistry B*, *102*(36), 6958–6967. https://doi.org/10.1021/jp9809787

Hodak, Jose H, Henglein, A., & Hartland, G. V. (2000). Photophysics of Nanometer Sized Metal

Particles : Electron-Phonon Coupling and. *The Journal of Physical Chemistry B, 104*(43), 9954–9965. Retrieved from http://pubs.acs.org/doi/abs/10.1021/jp002256x

Hollamby, M. J., Tabor, R., Mutch, K. J., Trickett, K., Eastoe, J., Heenan, R. K., & Grillo, I. (2008). Surfactants, *23*(8), 12235–12240.

Hou, M. J., Kim, M., & Shah, D. O. (1988). Hou 1.pdf. *Journal of Colloid and Interface Science*.

Huang, H. C., Rege, K., & Heys, J. J. (2010). Spatiotemporal temperature distribution and cancer cell death in response to extracellular hyperthermia induced by gold nanorods. *ACS Nano*, *4*(5), 2892–2900. https://doi.org/10.1021/nn901884d

Huang, J. S., Safran, S. A., Kim, M. W., Grest, G. S., Kotlarchyk, M., & Quirke, N. (1984). Attractive Interactions in Micelles and Microemulsions. *Physical Review Letters*, *53*(6), 592–595. https://doi.org/10.1103/PhysRevLett.53.592

Huang, X., Jain, P. K., El-Sayed, I. H., & El-Sayed, M. A. (2008). Plasmonic photothermal therapy (PPTT) using gold nanoparticles. *Lasers in Medical Science*, *23*(3), 217–228. https://doi.org/10.1007/s10103-007-0470-x

Huang, X., Qian, W., El-Sayed, I. H., & El-Sayed, M. A. (2007). The potential use of the enhanced nonlinear properties of gold nanospheres in photothermal cancer therapy. *Lasers in Surgery and Medicine*, *39*(9), 747–753. https://doi.org/10.1002/lsm.20577

Huo, S., Jin, S., Ma, X., Xue, X., Yang, K., Kumar, A., … Liang, X. J. (2014). Ultrasmall gold nanoparticles as carriers for nucleus-based gene therapy due to size-dependent nuclear entry. *ACS Nano*, *8*(6), 5852–5862. https://doi.org/10.1021/nn5008572

Ipe, B. I., George Thomas, K., Barazzouk, S., Hotchandani, S., & Kamat, P. V. (2002). Photoinduced charge separation in a fluorophore - Gold nanoassembly. *Journal of Physical Chemistry B*, *106*(1), 18–21. https://doi.org/10.1021/jp0134695

Jain, P. K., Huang, X., El-sayed, I. H., & El-sayed, M. A. (2008). Noble Metals on the Nanoscale : Optical and Photothermal Properties and Some Applications. *Accounts of Chemical*

Research, *41*(12), 7–9. https://doi.org/10.1021/ar7002804

Jain, P., Lee, K., & El-Sayed, I. (2006). Calculated absorption and scattering of gold nanoparticles of different size, shape, and composition. *The Journal of Physical Chemistry B*, *110*, 723038–727248. https://doi.org/10.1021/jp057170o

Jana, N. R., Gearheart, L., Obare, S. O., & Murphy, C. J. (2002). Anisotropic chemical reactivity of gold spheroids and nanorods. *Langmuir*, *18*(3), 922–927. https://doi.org/10.1021/la0114530

Jang, B., Park, J., Tung, C., Kim, I., & Choi, Y. (2011). Gold Nanorod - Photosensitizer, (2), 1086–1094.

Jaque, D., Martínez Maestro, L., del Rosal, B., Haro-Gonzalez, P., Benayas, A., Plaza, J. L., … García Solé, J. (2014). Nanoparticles for photothermal therapies. *Nanoscale*, *6*(16), 9494–9530. https://doi.org/10.1039/c4nr00708e

Keh, E., & Valeur, B. (1981). Investigation of water-containing inverted micelles by fluorescence polarization. Determination of size and internal fluidity. *Journal of Colloid And Interface Science*, *79*(2), 465–478. https://doi.org/10.1016/0021-9797(81)90098-9

Kelly, K. L., Coronado, E., Zhao, L. L., & Schatz, G. C. (2003). The optical properties of metal nanoparticles: The influence of size, shape, and dielectric environment. *Journal of Physical Chemistry B*, *107*(3), 668–677. https://doi.org/10.1021/jp026731y

Kepp, O., Galluzzi, L., Lipinski, M., Yuan, J., & Kroemer, G. (2011). Cell death assays for drug discovery. *Nature Reviews Drug Discovery*, *10*(3), 221–237. https://doi.org/10.1038/nrd3373

Khlebtsov, B., Zharov, V., Melnikov, A., Tuchin, V., & Khlebtsov, N. (2006). Optical amplification of photothermal therapy with gold nanoparticles and nanoclusters. *Nanotechnology*, *17*(20), 5167–5179. https://doi.org/10.1088/0957-4484/17/20/022

Kitchens, C. L., McLeod, M. C., & Roberts, C. B. (2003). Solvent Effects on the Growth and Steric Stabilization of Copper Metallic Nanoparticles in AOT Reverse Micelle Systems. *The*

Journal of Physical Chemistry B, *107*(41), 11331–11338. https://doi.org/10.1021/jp0354090

Kreke, P. J., Magid, L. J., & Gee, J. C. (2002). 1 H and 13 C NMR Studies of Mixed Counterion, Cetyltrimethylammonium Bromide/Cetyltrimethylammonium Dichlorobenzoate, Surfactant Solutions: The Intercalation of Aromatic Counterions . *Langmuir*, *12*(3), 699–705. https://doi.org/10.1021/la9509662

Kuo, W. S., Chang, Y. T., Cho, K. C., Chiu, K. C., Lien, C. H., Yeh, C. S., … Ahmad, I. (2012). Induction of ROS, mitochondrial damage and autophagy in lung epithelial cancer cells by iron oxide nanoparticles. *Biomaterials*, *33*(20), 2246–2249. https://doi.org/10.1016/j.biomaterials.2012.01.035

Kuo, W. S., Chang, Y. T., Cho, K. C., Chiu, K. C., Lien, C. H., Yeh, C. S., & Chen, S. J. (2012). Gold nanomaterials conjugated with indocyanine green for dual-modality photodynamic and photothermal therapy. *Biomaterials*, *33*(11), 3270–3278. https://doi.org/10.1016/j.biomaterials.2012.01.035

Lane, J. D., Allan, V. J., & Woodman, P. G. (2005). Active relocation of chromatin and endoplasmic reticulum into blebs in late apoptotic cells. *Journal of Cell Science*, *118*(17), 4059–4071. https://doi.org/10.1242/jcs.02529

Lang, J., Mascolo, G., Zana, R., & Luisi, P. L. (1990). Structure and dynamics of cetyltrimethylammonium bromide water-in-oil microemulsions. *Journal of Physical Chemistry*, *94*(7), 3069–3074. https://doi.org/10.1021/j100370a060

Langer, J., Novikov, S. M., & Liz-Marzán, L. M. (2015). Sensing using plasmonic nanostructures and nanoparticles. *Nanotechnology*, *26*(32), 322001. https://doi.org/10.1088/0957-4484/26/32/322001

Langevin, D. (1988). Microemulsions, *2*(7), 255–260.

Lee, J., Yang, J., Kwon, S. G., & Hyeon, T. (2016). Nonclassical nucleation and growth of inorganic nanoparticles. *Nature Reviews Materials*, *1*(8). https://doi.org/10.1038/natrevmats.2016.34

Lee, M. S., Park, S. S., Lee, G. D., Ju, C. S., & Hong, S. S. (2005). Synthesis of TiO2 particles by reverse microemulsion method using nonionic surfactants with different hydrophilic and hydrophobic group and their photocatalytic activity. *Catalysis Today*, *101*(3-4 SPEC. ISS.), 283–290. https://doi.org/10.1016/j.cattod.2005.03.018

Lemaire, B., Bothorel, P., & Roux, D. (1983). Micellar interactions in water-in-oil microemulsions. 1. Calculated interaction potential. *Journal of Physical Chemistry*, *87*(6), 1023–1028. https://doi.org/10.1021/j100229a021

Leonidova, A., Pierroz, V., Rubbiani, R., Lan, Y., Schmitz, A. G., Kaech, A., … Gasser, G. (2014). Photo-induced uncaging of a specific Re(i) organometallic complex in living cells. *Chemical Science*, *5*(10), 4044–4056. https://doi.org/10.1039/c3sc53550a

Li, G., Li, D., Zhang, L., Zhai, J., & Wang, E. (2009). One-step synthesis of folic acid protected gold nanoparticles and their receptor-mediated intracellular uptake. *Chemistry - A European Journal*, *15*(38), 9868–9873. https://doi.org/10.1002/chem.200900914

Li, Q., Li, T., Wu, J., & Zhou, N. (2000). Comparative study on the structure of water in reverse micelles stabilized with sodium bis(2-ethylhexyl) sulfosuccinate or sodium bis(2-ethylhexyl) phosphate in n-heptane. *Journal of Colloid and Interface Science*, *229*(1), 298–302. https://doi.org/10.1006/jcis.2000.7030

Lin, C., Lee, C., Hsieh, J., & Wang, H. (2009). Review: Synthesis of fluorescent metallic nanoclusters toward biomedical application: recent progress and present challenges. *J Med Biol …*, *29*(6), 276–283. https://doi.org/10.1021/jp0516846

Lin, J., Zhou, W., letters, C. O.-M., & 2001, undefined. (n.d.). Formation of ordered arrays of gold nanoparticles from CTAB reverse micelles. *Elsevier*. Retrieved from https://www.sciencedirect.com/science/article/pii/S0167577X00003852

Liu, H., Huang, G. W., Zhang, X. M., Ren, D. L., & Wilson, J. X. (2010). Folic acid supplementation stimulates notch signaling and cell proliferation in embryonic neural stem cells. *Journal of Clinical Biochemistry and Nutrition*, *47*(2), 174–180.

https://doi.org/10.3164/jcbn.10-47

Loo, C., Hirsch, L., Lee, M., Chang, E., West, J., Halas, N., & Drezek, R. (2005). Optics Letters 1012 (2005).Pdf, *30*(9), 1012–1014.

Lopez-quintela, M. A. (2003). Synthesis of nanomaterials in microemulsions : formation mechanisms and growth control □, *8*, 137–144. https://doi.org/10.1016/S1359-0294

López-Quintela, M. A., Rivas, J., Blanco, M. C., & Tojo, C. (2006). Synthesis of Nanoparticles in Microemulsions. In *Nanoscale Materials* (pp. 135–155). https://doi.org/10.1007/0-306-48108-1_6

López-Quintela, M. A., Tojo, C., Blanco, M. C., García Rio, L., & Leis, J. R. (2004). Microemulsion dynamics and reactions in microemulsions. *Current Opinion in Colloid and Interface Science*, *9*(3–4), 264–278. https://doi.org/10.1016/j.cocis.2004.05.029

López-Quintela, M., Rivas, J., Blanco, M., materials, C. T.-N., & 2004, undefined. (n.d.). Synthesis of nanoparticles in microemulsions. *Springer*. Retrieved from https://link.springer.com/content/pdf/10.1007/0-306-48108-1_6.pdf

Lu, Y., & Low, P. S. (2012). Folate-mediated delivery of macromolecular anticancer therapeutic agents. *Advanced Drug Delivery Reviews*, *64*(SUPPL.), 342–352. https://doi.org/10.1016/j.addr.2012.09.020

Lutz-Bueno, V., Pasquino, R., Liebi, M., Kohlbrecher, J., & Fischer, P. (2016). Viscoelasticity Enhancement of Surfactant Solutions Depends on Molecular Conformation: Influence of Surfactant Headgroup Structure and Its Counterion. *Langmuir*, *32*(17), 4239–4250. https://doi.org/10.1021/acs.langmuir.6b00776

Martin, S. J., Henry, C. M., & Cullen, S. P. (2012). A Perspective on Mammalian Caspases as Positive and Negative Regulators of Inflammation. *Molecular Cell*, *46*(4), 387–397. https://doi.org/10.1016/j.molcel.2012.04.026

Melamed, J. R., Edelstein, R. S., & Day, E. S. (2015). Elucidating the fundamental mechanisms of cell death triggered by photothermal therapy. *ACS Nano*, *9*(1), 6–11. https://doi.org/10.1021/acsnano.5b00021

Mendes, R., Pedrosa, P., Lima, J. C., Fernandes, A. R., & Baptista, P. V. (2017). Photothermal enhancement of chemotherapy in breast cancer by visible irradiation of Gold Nanoparticles. *Scientific Reports*, *7*(1), 1–9. https://doi.org/10.1038/s41598-017-11491-8

Mentel, T. F., & Luck, W. A. P. (2005). Pressure dependence of hydroxyl stretching vibrations. 2. Complexes of perfluoro-tert-butyl alcohol with aromatic acceptors. *The Journal of Physical Chemistry*, *95*(1), 68–74. https://doi.org/10.1021/j100154a017

Metiu, H. (1984). Surface enhanced spectroscopy. *Progress in Surface Science*, *17*(3–4), 153–320. https://doi.org/10.1016/0079-6816(84)90017-0

Mie, G. (1908). On the optics of turbid media, especially colloidal metal solutions. *Ann. Phys. Berlin*, *25*(3), 377–445.

Mieszawska, A. J., Mulder, W. J. M., Fayad, Z. A., & Cormode, D. P. (2013). Multifunctional gold nanoparticles for diagnosis and therapy of disease. *Molecular Pharmaceutics*, *10*(3), 831–847. https://doi.org/10.1021/mp3005885

Mills, A. J., Wilkie, J., & Britton, M. M. (2014). NMR and molecular dynamics study of the size, shape, and composition of reverse micelles in a cetyltrimethylammonium bromide (CTAB)/n-hexane/pentanol/water microemulsion. *Journal of Physical Chemistry B*, *118*(36), 10767–10775. https://doi.org/10.1021/jp504585k

Misra, R., Acharya, S., & Sahoo, S. K. (2010). Cancer nanotechnology: Application of nanotechnology in cancer therapy. *Drug Discovery Today*, *15*(19–20), 842–850. https://doi.org/10.1016/j.drudis.2010.08.006

Mocanu, A., Cernica, I., Tomoaia, G., Bobos, L. D., Horovitz, O., & Tomoaia-Cotisel, M. (2009). Self-assembly characteristics of gold nanoparticles in the presence of cysteine. *Colloids and Surfaces A: Physicochemical and Engineering Aspects*, *338*(1–3), 93–101. https://doi.org/10.1016/j.colsurfa.2008.12.041

Moilanen, D. E., Fenn, E. E., Wong, D., & Fayer, M. D. (2009). Water dynamics in large and small reverse micelles: From two ensembles to collective behavior. *Journal of Chemical Physics*, *131*(1). https://doi.org/10.1063/1.3159779

Montalti, M., Prodi, L., Zaccheroni, N., & Battistini, G. (2004). Modulation of the photophysical properties of gold nanoparticles by accurate control of the surface coverage. *Langmuir*, *20*(18), 7884–7886. https://doi.org/10.1021/la0491044

Myakonkaya, O., Eastoe, J., Mutch, K. J., Rogers, S., Heenan, R., & Grillo, I. (2009). Control over microemulsions with solvent blends. *Langmuir*, *25*(5), 2743–2748. https://doi.org/10.1021/la8037507

Nazir, S., Hussain, T., Ayub, A., Rashid, U., & MacRobert, A. J. (2014). Nanomaterials in combating cancer: Therapeutic applications and developments. *Nanomedicine: Nanotechnology, Biology, and Medicine*, *10*(1), 19–34. https://doi.org/10.1016/j.nano.2013.07.001

Neouze, M. A., & Schubert, U. (2008). Surface modification and functionalization of metal and metal oxide nanoparticles by organic ligands. *Monatshefte Fur Chemie*, *139*(3), 183–195. https://doi.org/10.1007/s00706-007-0775-2

Onori, G., & Santucci, A. (1993). IR investigations of water structure in aerosol OT reverse micellar aggregates. *Journal of Physical Chemistry*, *97*(20), 5430–5434. https://doi.org/10.1021/j100122a040

Pan, Y., Neuss, S., Leifert, A., Fischler, M., Wen, F., Simon, U., … Jahnen-Dechent, W. (2007). Size-dependent cytotoxicity of gold nanoparticles. *Small*, *3*(11), 1941–1949. https://doi.org/10.1002/smll.200700378

Parak, W. (2008). 2008 Gold : Chemistry , Materials and Catalysis Issue Please take a look at the full table of contents to access the. *Chemical Society Reviews*, *37*(9), 1909–1930. https://doi.org/10.1590/S0100-40422013000300006

Park, S., Moilanen, D. E., & Fayer, M. D. (2008). Water dynamics-The effects of ions and nanoconfinement. *Journal of Physical Chemistry B, 112*(17), 5279–5290. https://doi.org/10.1021/jp7121856

Parker, N., Turk, M. J., Westrick, E., Lewis, J. D., Low, P. S., & Leamon, C. P. (2005). Folate receptor expression in carcinomas and normal tissues determined by a quantitative radioligand binding assay. *Analytical Biochemistry*, *338*(2), 284–293. https://doi.org/10.1016/j.ab.2004.12.026

Pasparakis, G. (2013). Light-induced generation of singlet oxygen by naked gold nanoparticles and its implications to cancer cell phototherapy. *Small*, *9*(24), 4130–4134. https://doi.org/10.1002/smll.201301365

Pentanol, M., Palazzo, G., Lopez, F., Giustini, M., Colafemmina, G., & Ceglie, A. (2003). Role of the Cosurfactant in the CTAB / Water / n-Pentanol / n-Hexane Water-in-Oil. *Society*, 1924–1931. https://doi.org/10.1021/jp026430o

Personick, M. L., Langille, M. R., Zhang, J., Harris, N., Schatz, G. C., & Mirkin, C. A. (2011). Synthesis and Isolation of {110}-Faceted Gold Bipyramids and Rhombic Dodecahedra. *Journal of the American Chemical Society*, *133*(16), 6170–6173. https://doi.org/10.1021/ja201826r

Pileni, M. P. (2006). Reverse micelles used as templates: A new understanding in nanocrystal growth. *Journal of Experimental Nanoscience*, *1*(1), 13–27. https://doi.org/10.1080/17458080500462075

Pileni, M. P. (2007). Control of the size and shape of inorganic nanocrystals at various scales from nano to macrodomains. *Journal of Physical Chemistry C*, *111*(26), 9019–9038. https://doi.org/10.1021/jp070646e

Pinilla, A. M., Blach, D., Mendez, S. C., & Ortega, F. M. (2019). AOT direct and reverse micelles as a reaction media for anisotropic silver nanoparticles functionalized with folic acid as a photothermal agent on HeLa cells. *SN Applied Sciences*, *1*(8). https://doi.org/10.1007/s42452-019-0894-5

Pissuwan, D., Valenzuela, S. M., & Cortie, M. B. (2006). Therapeutic possibilities of plasmonically heated gold nanoparticles. *Trends in Biotechnology*, *24*(2), 62–67. https://doi.org/10.1016/j.tibtech.2005.12.004

Porta, F., Prati, L., Rossi, M., & Scari, G. (2002). Synthesis of Au(0) nanoparticles from W/O microemulsions. *Colloids and Surfaces A: Physicochemical and Engineering Aspects*, *211*(1), 43–48. https://doi.org/10.1016/S0927-7757(02)00220-0

Pramanik, S., Bhattacharya, S. C., & Imae, T. (2007). Fluorescence quenching of 3,7-diamino-2,8-dimethyl-5-phenyl phenazinium chloride by AgCl and Ag nanoparticles. *Journal of Luminescence*, *126*(1), 155–159. https://doi.org/10.1016/j.jlumin.2006.06.008

Rai, A., Singh, A., Ahmad, A., & Sastry, M. (2006). Role of halide ions and temperature on the morphology of biologically synthesized gold nanotriangles. *Langmuir*, *22*(2), 736–741. https://doi.org/10.1021/la052055q

Rayavarapu, R. G., Petersen, W., Ungureanu, C., Post, J. N., Van Leeuwen, T. G., & Manohar, S. (2007). Synthesis and bioconjugation of gold nanoparticles as potential molecular probes for light-based imaging techniques. *International Journal of Biomedical Imaging, 2007*. https://doi.org/10.1155/2007/29817

Reviews, A., & Langevin, D. (1992). *MICELLES AND MICROEMULSIONS D.*

Reviews, V. R.-R. C., & 2000, undefined. (n.d.). Quantum-size colloid metal systems. *Pubs.Rsc.Org*. Retrieved from https://pubs.rsc.org/en/content/articlehtml/2000/rc/rc000821

Rhee, S. G. (2006). H2O2, a necessary evil for cell signaling. *Science*, *312*(5782), 1882–1883. https://doi.org/10.1126/science.1130481

Richardson, H. H., Carlson, M. T., Tandler, P. J., Hernandez, P., & Govorov, A. O. (2009). Experimental and theoretical studies of light-to-heat conversion and collective heating effects in metal nanoparticle solutions. *Nano Letters*, *9*(3), 1139–1146. https://doi.org/10.1021/nl8036905

Rosi, N. L., Giljohann, D. A., Thaxton, C. S., Lytton-Jean, A. K. R., Han, M. S., & Mirkin, C. A. (2006). Oligonucleotide-modified gold nanoparticles for infracellular gene regulation. *Science*, *312*(5776), 1027–1030. https://doi.org/10.1126/science.1125559

Ryter, S. W., Kim, H. P., Hoetzel, A., Park, J. W., Nakahira, K., Wang, X., & Choi, A. M. K. (2007). Mechanisms of Cell Death in Oxidative Stress. *Antioxidants & Redox Signaling*, *9*(1), 49–89. https://doi.org/10.1089/ars.2007.9.49

Sabharanjak, S., & Mayor, S. (2004). Folate receptor endocytosis and trafficking. *Advanced Drug Delivery Reviews*, *56*(8), 1099–1109. https://doi.org/10.1016/j.addr.2004.01.010

Salabat, A., Eastoe, J., Mutch, K. J., & Tabor, R. F. (2008). Tuning aggregation of microemulsion droplets and silica nanoparticles using solvent mixtures. *Journal of Colloid and Interface Science*, *318*(2), 244–251. https://doi.org/10.1016/j.jcis.2007.10.050

Sau, T. K., Rogach, A. L., Jäckel, F., Klar, T. A., & Feldmann, J. (2010). Properties and applications of colloidal nonspherical noble metal nanoparticles. *Advanced Materials*, *22*(16), 1805–1825. https://doi.org/10.1002/adma.200902557

SCENIHR. (2006). SCENIHR Modified opinion on The appropriateness of existing methodologies to assess the potential risks associated with engineered and adventitious. *Knowledge Creation Diffusion Utilization*, (March).

Schmitt, J., Mächtle, P., Eck, D., Möhwald, H., & Helm, C. A. (1999). Preparation and Optical Properties of Colloidal Gold Monolayers. *Langmuir*, *15*(9), 3256–3266. https://doi.org/10.1021/la981078k

Schneider, G., Decher, G., Nerambourg, N., Praho, R., Werts, M. H. V., & Blanchard-Desce, M. (2006). Distance-dependent fluorescence quenching on gold nanoparticles ensheathed with layer-by-layer assembled polyelectrolytes. *Nano Letters*, *6*(3), 530–536. https://doi.org/10.1021/nl052441s

Song, C. W. (1984). Effect of local hyperthermia on blood flow and microenvironment: a review. *Cancer Research*, *44*(10 Suppl), 4721s-4730s. Retrieved from http://www.ncbi.nlm.nih.gov/pubmed/6467226

Song, J., Kim, S., Doh, H., Jung, S., Nam, J., & Hwang, S. (2014). Gold nanoparticle-mediated photothermal therapy: current status and future perspective. *Nanomedicine*, *9*(13), 2003–2022. https://doi.org/10.2217/nnm.14.147

Soon Gu Kwon,† Yuanzhe Piao,† Jongnam Park,† Subramanian Angappane,‡ Younghun Jo,§ Nong-Moon Hwang,| Je-Geun Park, and T. H. (2003). Kinetics of Monodisperse Iron Oxide Nanocrystal Formation by “Heating-Up” Process Soon, (c), 2002–2003. https://doi.org/10.1021/ja074633q

Sudeep, P. K., Joseph, S. T. S., & Thomas, K. G. (2005). Selective detection of cysteine and glutathione using gold nanorods. *Journal of the American Chemical Society*, *127*(18), 6516–6517. https://doi.org/10.1021/ja051145e

Sun, C., Sze, R., & Zhang, M. (2006). Folic acid-PEG conjugated superparamagnetic nanoparticles for targeted cellular uptake and detection by MRI. *Journal of Biomedical Materials Research Part A*, *78A*(3), 550–557. https://doi.org/10.1002/jbm.a.30781

Svaasand, L. O., Gomer, C. J., & Morinelli, E. (1990). On the physical rationale of laser induced hyperthermia. *Lasers in Medical Science*, *5*(2), 121–128. https://doi.org/10.1007/BF02031373

Szakács, Z., & Noszál, B. (2006). Determination of dissociation constants of folic acid, methotrexate, and other photolabile pteridines by pressure-assisted capillary electrophoresis. *Electrophoresis*, *27*(17), 3399–3409. https://doi.org/10.1002/elps.200600128

Taira, S., Hatanaka, T., Moritake, S., Kai, Y., Ichiyanagi, Y., & Setou, M. (2007). Cellular Recognition of Functionalized with Folic acid Nanoparticles. *E-Journal of Surface Science and Nanotechnology*, *5*(January), 23–28. https://doi.org/10.1380/ejssnt.2007.23

Teow, Y., & Valiyaveettil, S. (2010). Active targeting of cancer cells using folic acid-conjugated platinum nanoparticles. *Nanoscale*, *2*(12), 2607–2613. https://doi.org/10.1039/c0nr00204f

Thompson, D. T. (2007). Using gold nanoparticles for catalysis. *Nano Today*, *2*(4), 40–43. https://doi.org/10.1016/S1748-0132(07)70116-0

Tsoli, M., Kuhn, H., Brandau, W., Esche, H., & Schmid, G. (2005). Cellular Uptake and Toxicity of Au55 Clusters. *Small*, *1*(8–9), 841–844. https://doi.org/10.1002/smll.200500104

Turk, M. J., Reddy, J. A., Chmielewski, J. A., & Low, P. S. (2002). Characterization of a novel pH-sensitive peptide that enhances drug release from folate-targeted liposomes at endosomal pHs. *Biochimica et Biophysica Acta - Biomembranes*, *1559*(1), 56–68. https://doi.org/10.1016/S0005-2736(01)00441-2

Ulmius, J., & Wennerström, H. (1977). Proton NMR bandshapes for large aggregates; Micellar solutions of hexadecyltrimethylammonium bromide. *Journal of Magnetic Resonance (1969)*, *28*(2), 309–312. https://doi.org/10.1016/0022-2364(77)90161-5

USKOKOVIĆ, V., & DROFENIK, M. (2005). Synthesis of Materials Within Reverse Micelles. *Surface Review and Letters*, *12*(02), 239–277. https://doi.org/10.1142/s0218625x05007001

Van Santen, R. A. (1984). The Ostwald step rule. *Journal of Physical Chemistry*, *88*(24), 5768–5769. https://doi.org/10.1021/j150668a002

Vankayala, R., Kuo, C. L., Sagadevan, A., Chen, P. H., Chiang, C. S., & Hwang, K. C. (2013). Morphology dependent photosensitization and formation of singlet oxygen (^{1}Δ<inf>g</inf>) by gold and silver nanoparticles and its application in cancer treatment. *Journal of Materials Chemistry B*, *1*(35), 4379–4387. https://doi.org/10.1039/c3tb20806k

Vankayala, R., Sagadevan, A., Vijayaraghavan, P., Kuo, C. L., & Hwang, K. C. (2011). Metal nanoparticles sensitize the formation of singlet oxygen. *Angewandte Chemie - International Edition*, *50*(45), 10640–10644. https://doi.org/10.1002/anie.201105236

Velegol, S. B., Fleming, B. D., Biggs, S., Wanless, E. J., & Tilton, R. D. (2000). Counterion Effects on Hexadecyltrimethylammonium Surfactant Adsorption and Self-Assembly on Silica. *Langmuir*, *16*(6), 2548–2556. https://doi.org/10.1021/la9910935

Wang, C. C., Chen, D. H., & Huang, T. C. (2001). Synthesis of palladium nanoparticles in water-in-oil microemulsions. *Colloids and Surfaces A: Physicochemical and Engineering Aspects*, *189*(1–3), 145–154. https://doi.org/10.1016/S0927-7757(01)00576-3

Wang, X., Yang, L., Chen, Z., & Shin, D. M. (2008). Application of Nanotechnology in Cancer Therapy and Imaging. *CA: A Cancer Journal for Clinicians*, *58*(2), 97–110. https://doi.org/10.3322/ca.2007.0003

Wayland, B. B., & Drago, R. S. (1964). Determination of the Donor Sites in Lewis Acid Adducts of Anisole and Thioanisole. *Journal of the American Chemical Society*, *86*(23), 5240–5244. https://doi.org/10.1021/ja01077a040

Wilcoxon, J. P., Williamson, R. L., & Baughman, R. (1993). Optical properties of gold colloids formed in inverse micelles. *The Journal of Chemical Physics*, *98*(12), 9933–9950. https://doi.org/10.1063/1.464320

Yang, P. H., Sun, X., Chiu, J. F., Sun, H., & He, Q. Y. (2005). Transferrin-mediated gold nanoparticle cellular uptake. *Bioconjugate Chemistry*, *16*(3), 494–496. https://doi.org/10.1021/bc049775d

Yen, H. J., Hsu, S. H., & Tsai, C. L. (2009). Cytotoxicity and immunological response of gold and silver nanoparticles of different sizes. *Small*, *5*(13), 1553–1561. https://doi.org/10.1002/smll.200900126

Yoo, D., Jeong, H., Preihs, C., Choi, J. S., Shin, T. H., Sessler, J. L., & Cheon, J. (2012). Double-effector nanoparticles: A synergistic approach to apoptotic hyperthermia. *Angewandte Chemie - International Edition*, *51*(50), 12482–12485. https://doi.org/10.1002/anie.201206400

Zembruski, N. C. L., Stache, V., Haefeli, W. E., & Weiss, J. (2012). 7-Aminoactinomycin D for apoptosis staining in flow cytometry. *Analytical Biochemistry*, *429*(1), 79–81. https://doi.org/10.1016/j.ab.2012.07.005

Zhang, J., Rana, S., Srivastava, R. S., & Misra, R. D. K. (2008). On the chemical synthesis and drug delivery response of folate receptor-activated, polyethylene glycol-functionalized magnetite nanoparticles. *Acta Biomaterialia*, *4*(1), 40–48. https://doi.org/10.1016/j.actbio.2007.06.006

Zhu, D. M., Wu, X., & Schelly, Z. A. (1992). Investigation of the micropolarities in reverse micelles of triton X-100 in mixed solvents of benzene and n-hexane. *Journal of Physical Chemistry*, *96*(17), 7121–7126. https://doi.org/10.1021/j100196a053

Zimmermann, M., & Meyer, N. (2011). Annexin V/7-AAD Staining in Keratinocytes (pp. 57–63). https://doi.org/10.1007/978-1-61779-108-6_8

Appendices

Appendix A. Absorption spectra of AuNPs synthesized by *n*-hexane /1-butanol/CTAB RMs at A) $W_0 = 3$ and B) $W_0 = 10$, [CTAB] = 0.1 M, [1-butanol] = 6.5 M as a function of the reaction time. An empty CTAB RM solution was used as a blank.

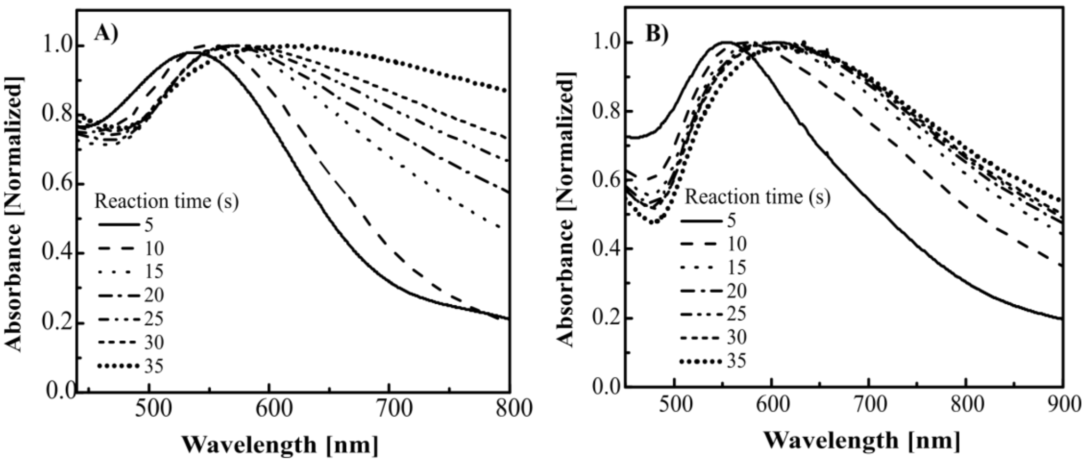

Appendix B. Absorption spectra of AuNPs synthesized by toluene /1-butanol/CTAB RMs at (A) $W_0 = 3$ and (B) $W_0 = 10$, [CTAB] = 0.1 M, [1-butanol] = 3.3 M as a function of the reaction time. An empty CTAB RM solution was used as a blank.

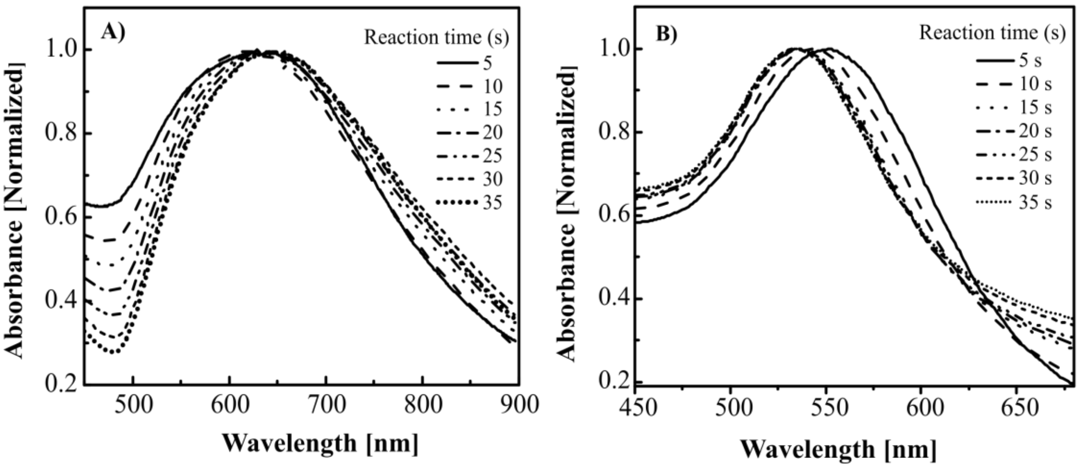

Appendix C. Cell viability assays of HeLa experimental control and laser control (cells exposed to 638 nm laser at 1.56 W/cm^2 power density for 5 min without AuNPs). The values represent the mean ± standard deviation of three independent experiments.

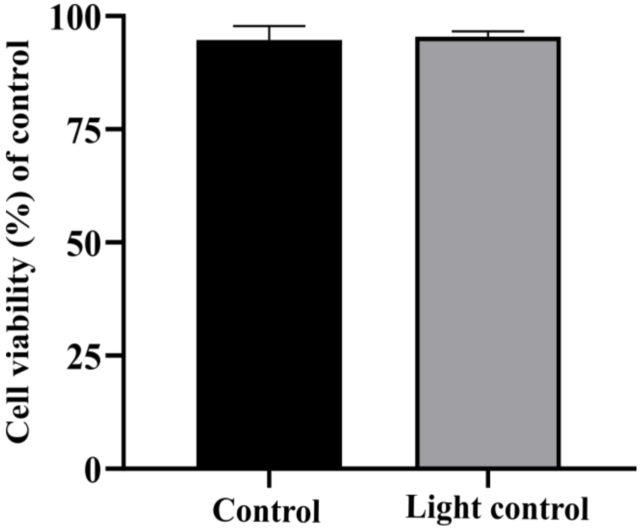

Appendix D. LSPR absorption bands of A) spherical AuNPs and B) anisotropic AuNPs in aqueous medium.

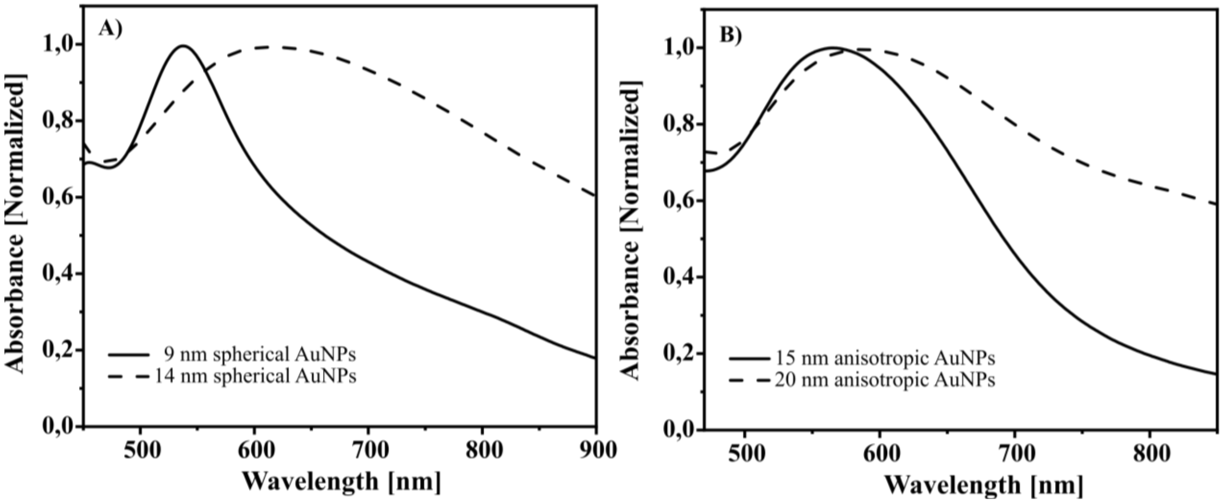

Appendix E. Temperature increase induced by Photothermal heating of spherical, anisotropic AuNPs solutions and control media (MEM) without AuNPs upon exposure to 638 nm laser excitation at 1.56 W/cm^2.

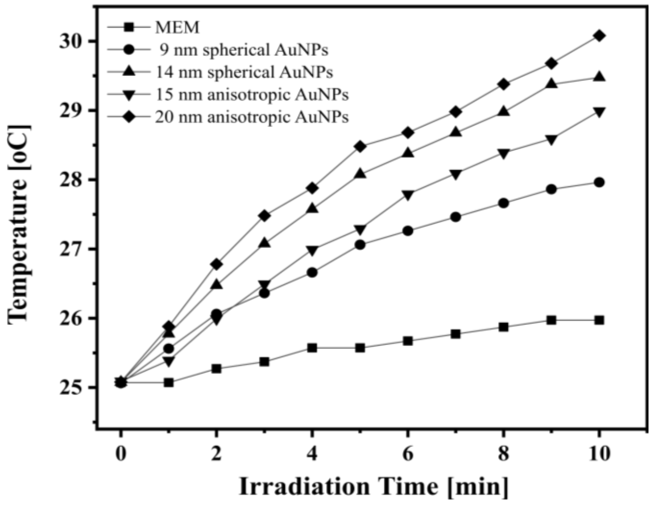

Appendix F. Differential interference contrast (DIC) images of HeLs cells treated with spherical and anisotropic AuNPs at 100 μM. White circles shows agglomerates of AuNPs decorated HeLa cells which increase as the particle size increases.

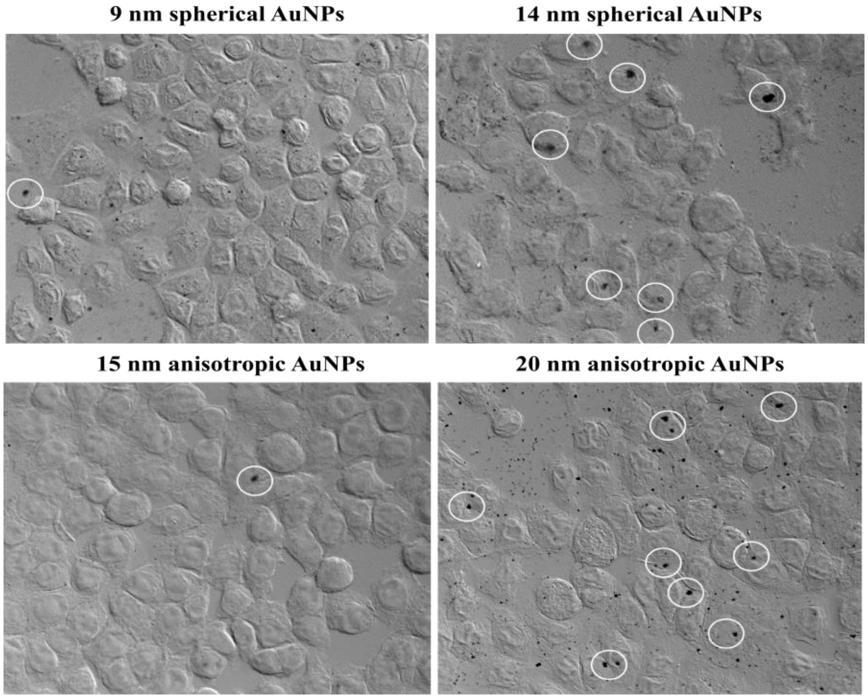

Appendix G. TEM images of FA-AuNPs distribution in Vero cells upon irradiation treatment with 630 nm at 1.56 W/cm^2 with 50 μM spherical and anisotropic FA-AuNPs: A) spherical FA-AuNPs of 9 nm, B) spherical FA-AuNPs of 14 nm, C) anisotropic FA-AuNPs of 15 nm and D) anisotropic FA-AuNPs of 20 nm. Electron-dense areas correspond to the FA-AuNPs (arrowhead).